Comparison of Approximate Riemann Solvers

Charlotte Kong

May 2011

Department of Mathematics
University of Reading

Supervisor: Dr P Sweby

A dissertation submitted in partial fulfilment of the requirement for the degree of Master of Science in Mathematical and Numerical Modelling of the Atmosphere and Oceans.

Declaration

I confirm that this is my own work, and the use of all material from other sources has been properly and fully acknowledged.

Charlotte Kong

Acknowledgements

I'd like to thank the Mathematics Department of the University of Reading for all their support. I'd like to thank my husband for patience and tea. The NERC for financial support. Author's Toro and LeVeque for making a complicated subject more accessible. Above all I'd like to thank Dr P Sweby for his patience and support.

Abstract

This paper presents a review on the numerical solution of the Euler equations. Four different high resolution schemes are considered: Roe's Riemann solver, the HLL and HLLC schemes and the Osher-Solomon solver. We present a comprehensive variety of one-dimensional test cases designed to test the accuracy and robustness of each scheme to first-order. Roe's scheme is also taken to second-order to demonstrate the desirability of high-order schemes. The results of all schemes are compared to discuss which scheme is most desirable. Overall no one scheme was determined to be the best, and further study was recommended.

Contents

List of Figures

1 Introduction

When solving systems of conservation laws, either by finite difference or finite volume techniques, it is usual to employ an approximate Riemann solver which it is hoped captures the main features of the Riemann problem solution whilst avoiding the complexity of the exact solution, even if available. Approximate solvers have developed due to the costly nature of the iterative exact schemes and the need to approximate certain areas. There are several such solvers available for this purpose, for example Roe, Osher-Solomon, HHL, HHLC, and so on. The aim of this study is to review some of the most popular approximate schemes and highlight their stengths and weaknesses.

The first part of this paper will look at the Euler equations and how they are formed and represented. We will then go on to discuss how the Euler equations become Riemann problems, and define exactly what a Riemann problem is. This will be followed by the introduction of some test problems which will be used to test numerous potential flaws in the schemes. The following section will look at the Godunov scheme. The Godunov scheme was founded in 1959, and the principles of which are the basis for the approximate Riemann solvers that will be investigated.

After this we will review some important points that need to be considered when using the schemes. These include the Courant coefficient, and then the time step size utilised when running the schemes and finally the boundary conditions used with the initial problems discussed in Section 2.3. Next we will look at the schemes themselves. The schemes chosen to investigate in this paper were the Roe solver, the HLL and its extension HLLC solvers, and finally the Osher-Solomon solver. A second order procedure is then presented, which will be used on the Roe solver. The next section presents the results of various numerical tests on the schemes. Following this is a discussion of the results and a conclusion summarising the findings of this study.

2 Fluid Dynamics and the Riemann Problem

The science of fluid dynamics concerns itself with the motion of fluids, that is liquids and gases, and has a wide range of applications including traffic flow and weather predictions. The foundations of fluid dynamics are the conservation laws, specifically those of conservation of mass, momentum and energy. For the purposes of testing approximate Riemann solvers, we concern ourselves with the Euler equations, those that govern inviscid flow. This section will introduce the Euler equations and their notation, before carrying on to introduce the Riemann problem itself. Following this specific test cases will be introduced that will be used to test solvers for potential weaknesses in the schemes. All equations will be presented in their one-dimensional form only, as further dimensions are beyond the scope of this investigation.

2.1 Euler Equations

The Euler equations govern inviscid flow; a fluid that is assumed to have no viscosity. They are concerned primarily with the conservation of mass, momentum and energy and correspond to the Navier-Stokes equations with zero viscosity and heat conduction terms. The equations are written in two different forms: *conservation* form and *non-conservation* form. We need only concern ourselves with the *conservation* form for this project, which emphasise the physical interpretation of the equations as conservation laws through a control volume fixed in space. Computationally, there are advantages to expressing the governing equations in terms of conserved variables: mass density ρ, the x-velocity component u and the total energy per unit mass E. These lead to numerical methods described as *conservative methods* [20]. To begin, we state the equations in terms of the conserved variables with the assumption that quantities involved are sufficiently smooth to allow for differentiation. Later we will remove the constraint to consider solutions containing discontinuities, such as shock waves.

$$\rho_t + (\rho u)_x = 0, \tag{2.1}$$

$$(\rho u)_t + (\rho u^2 + p)_x = 0, \tag{2.2}$$

$$E_t + [u(E + p)]_x = 0. \tag{2.3}$$

Here E is the total energy per unit volume

$$E = \rho\left(\tfrac{1}{2}\mathbf{V}^2 + e\right) \tag{2.4}$$

where

$$\tfrac{1}{2}\mathbf{V}^2 = \tfrac{1}{2}\mathbf{V}\cdot\mathbf{V} = \tfrac{1}{2}u^2$$

is the *specific kinetic energy* and e is the *specific internal energy.* The conservation laws (2.1)-(2.3) can be expressed in compact notation by defining a column vector $\mathbf{U}$ of conserved variables and the flux vector $\mathbf{F}(\mathbf{U})$ in the x directions. So (2.1)-(2.3) now read

$$\mathbf{U}_t + \mathbf{F}(\mathbf{U})_x = 0, \tag{2.5}$$

with

$$\left.\mathbf{U} = \begin{bmatrix} \rho \\ \rho u \\ E \end{bmatrix}, \quad \mathbf{F} = \begin{bmatrix} \rho u \\ \rho u^2 + p \\ u(E+p) \end{bmatrix}\right\} \tag{2.6}$$

The flux vector $\mathbf{F} = \mathbf{F}(\mathbf{U})$ equations are to be regarded as functions of the conserved variable vector $\mathbf{U}$.

2.2 The Riemann Problem

The *Riemann problem* consists of a conservation law together with piecewise constant data having a single discontinuity. Here we will discuss the problem for a linear system, and then discuss how the Riemann problem for the Euler equations, addressing specific problems that will be focused on during comparisons of schemes.

The initial state of the system is defined as

$$u(x, t=0) = \begin{cases} u_L \text{ for } x \leqslant 0 \\ u_R \text{ for } x \geqslant 0 \end{cases}. \tag{2.7}$$

To put (2.7) in words: the initial state is constant for all negative x, and constant for all positive x, but differs between left and right. In the one-dimensional case we can consider this problem as a gas with one temperature and density located to the left of a removable wall and another gas with another temperature and density to the right of the wall. At time $t = 0$ the wall is instantly removed and the results are observed.

In numerical analysis Riemann problems appear in a natural way in finite volume methods for the solution of conservation law equations due to the discreteness of the grid. For this we use approximate Riemann solvers, since iterative schemes are too costly some assumptions must be made, which will be discussed further in the following section. First this subsection will consider various types of Riemann problems which will be used to test the approximate Riemann solvers.

2.3 Specific Riemann Problems

To discuss specific Riemann problems we must first introduce some concepts: shocks, rarefactions and contacts. These are all types of discontinuities which we can describe using the example of traffic flow. A *shock wave* is where density increases and velocity decreases very suddenly, for example, drivers moving fast through light traffic applying their breaks suddenly. A *rarefaction wave* occurs where the fluid is becoming more rarefied as the density decreases, for example, as cars move out of a congested region, they accelerate smoothly and density in turn decreases smoothly. Contact discontinuities are surfaces that separate zones of different density and temperature, they are in pressure equilibrium and no gas flows across. We look for specific known problems containing the types of discontinuities mentioned in order to test the effectiveness of the approximate Riemann solver schemes considered.

2.3.1 Sod's Shock Tube

Sod's shock tube problem [15] is a common test for the accuracy of Riemann solvers and therefore invaluable to this study. The tests consists of a one-dimensional Riemann problem with the following parameters

$$\begin{pmatrix} \rho_L \\ p_L \\ u_L \end{pmatrix} = \begin{pmatrix} 1.0 \\ 1.0 \\ 0.0 \end{pmatrix}, \quad \begin{pmatrix} \rho_R \\ p_R \\ u_R \end{pmatrix} = \begin{pmatrix} 0.125 \\ 0.1 \\ 0.0 \end{pmatrix}. \tag{2.8}$$

This problem can be described using the Euler equations for its time evolution. This leads to three characteristics describing the propagation speed of the different regions of the system. These are the rarefaction wave, the contact discontinuity and the shock discontinuity. Solving this numerically it gives information on how well a scheme captures and resolves shocks and contact discontinuities and how well the correct density of the rarefaction wave is reproduced. This will be used as the main test for the schemes.

2.3.2 Blast Wave

The Blast Wave Problem we use here was presented by Woodward Collela [22] and represents the pressure and flow resulting from the deposition of a large amount of energy in a small very localised volume. For the purposes of this study we will split the blast tube problem into two: left hand and right hand sides, as it is easier to find the exact solution this way. The parameters for this equation are as follows

$$\rho(x,0)=1,\ p(x,0)=\begin{cases}1000\ if\ 0<x<0.1,\\ 0.1\ if\ 0.1<x<0.9,\\ 100\ if\ 0.9<x<1,\end{cases}\ \text{and}\ u(x,0)=0. \tag{2.9}$$

This is a very severe test problem, the left half containing a left rarefaction, a contact and a right shock, and the right half containing a left shock, a contact discontinuity and a right rarefaction. Walls are present at either side of the domain for this test case, so we would want to use reflecting boundary conditions. The boundary conditions will be discussed in the next section.

2.3.3 The 123 Problem

The next problem is known as the *123 problem* and was presented by Einfeld *et al.* [5], with the following parameters,

$$\rho(x,0)=1,\ p(x,0)=0.4,\ \text{and}\ u(x,0)=\begin{cases}-2\ if\ x<0.5,\\ 2\ if\ x\geqslant 0.5.\end{cases} \tag{2.10}$$

The solution of this problem consists of two strong rarefactions and a trivial stationary contact discontinuity. The intermediate state pressure p_* is very small, close to vacuum, and this can lead to difficulties in the iteration scheme to find p_* numerically.

2.3.4 Other Problems

The last test is made up of right and left shocks emerging from the solution to the left and right sections of the blast wave problem. It has the following parameters

$$\rho(x,0) = 5.99924,\ p(x,0) = \begin{cases} 460.894\ if\ x < 0.5 \\ 46.0950\ if\ x \geqslant 0.5 \end{cases},\ \text{and}\ u(x,0) = \begin{cases} 19.5975\ if\ x < 0.5, \\ \text{-}\ 6.19633\ if\ x \geqslant 0.5. \end{cases} \tag{2.11}$$

The solution of this represents the collision of these two strong shocks and consists of a left facing shock travelling slowly to the right, a right travelling contact discontinuity and a right travelling shock wave.

3 Godunov's Method

The original concept of flux algorithms based on exact or approximate solutions of the Riemann problem was first developed by Godunov [6]. In this paper, Godunov introduced utilising the solution of the local Riemann problem at each cell face as the basis for determining the flux $\mathbf{F}_{i\pm\frac{1}{2}}$ in the integral form of the Euler equations

$$\mathbf{U}_i^{n+1} = \mathbf{U}_i^n - \frac{1}{\Delta x}\int_t^{t^{n+1}} (\mathbf{F}_{i+\frac{1}{2}} - \mathbf{F}_{i-\frac{1}{2}})dt. \tag{3.1}$$

Firstly we can think of the solution $\mathbf{U}_i$ for $i = 1, ..., M$ at time t^n. In general there is a discontinuity in U_i at every cell face. The flux $\mathbf{F}_{i+\frac{1}{2}}$ is then determined from the solution of the local general Riemann problem at $x_{i+\frac{1}{2}}$. The left and right hand states $\mathbf{U}^L_{i+\frac{1}{2}}$ and $\mathbf{U}^R_{i+\frac{1}{2}}$ at $x_{i+\frac{1}{2}}$ can be taken as

$$\begin{aligned} \mathbf{U}^l_{i+\frac{1}{2}} &= \mathbf{U}_i \\ \mathbf{U}^l_{i+\frac{1}{2}} &= \mathbf{U}_{i+1}, \end{aligned} \tag{3.2}$$

which corresponds to a first-order accuracte reconstruction of $\mathbf{U}$ to the cell face. The solution to the general Riemann problem at $x_{i+\frac{1}{2}}$ for $t > t^n$ does not depend on x or t separately but rather only on $(x - x_{i+\frac{1}{2}}/(t - t^n)$. A consequence of this is the solution for $\mathbf{U}$ at $x_{i+\frac{1}{2}}$ is time-independent, thus

$$\int_t^{t^{n+1}} \mathbf{F}_{i+\frac{1}{2}} dt = \mathbf{F}_{i+\frac{1}{2}} \Delta t = \Im\left(\mathbf{U}^R_{i+\frac{1}{2}}\right)\Delta t, \tag{3.3}$$

where $\mathbf{U}^R_{i+\frac{1}{2}}$ is the solution of the general Riemann problem at $x_{i+\frac{1}{2}}$ using (3.2). This also holds for $\mathbf{F}_{i+\frac{1}{2}}$. Therefore we have

$$\mathbf{U}_i^{n+1} = \mathbf{U}_i^n - \frac{\Delta t}{\Delta x}(\Im(\mathbf{U}^R_{i+\frac{1}{2}}) - \Im(\mathbf{U}^R_{i-\frac{1}{2}}).) \tag{3.4}$$

The Godunov method can also be written in the conservative form

$$\mathbf{U}_i^{n+1} = \mathbf{U}_i^n + \frac{\Delta t}{\Delta x}\left[\mathbf{F}_{i-\frac{1}{2}} - \mathbf{F}_{i+\frac{1}{2}}\right], \tag{3.5}$$

where the intercell numerical flux is given by

$$\mathbf{F}_{i+\frac{1}{2}} = \mathbf{F}(\mathbf{U}_{i+\frac{1}{2}}(0)), \tag{3.6}$$

if the time step Δt satisfies the condition

$$\Delta t \leqslant \frac{\Delta x}{S^n_{\max}}. \tag{3.7}$$

where $S^n_{\max}$ is the maximum wave velocity present through the velocity at time t^n [20]. More on the choice of time step size will be presented in the following sections.

4 Approximate Riemann Solvers

This chapter will briefly introduce some concepts needed for approximate Riemann solvers. It will also provide useful information on the structure of approximate programs, how time step size is chosen and so on.

4.1 Courant Coefficient

At this stage it is necessary to introduce the Courant or CFL coefficient, a ratio that will prove invaluable when seeking accuracy from the solvers. The CFL condition is a necessary condition that must be satisfied by any finite volume or finite difference method in order to provide stability and hence convergence to the solution of a differential equation as the grid is refined. Leveque summarised the condition as

CFL Condition : A numerical method can be convergent only if its numerical domain of dependence contains the the true domain of dependence of the PDE, at least in the limit Δt and Δx go to zero [8].

While it is a necessary condition, it is not always sufficient alone to guarantee stability.

4.2 Time Step Size

It is necessary to choose a time step Δt that ensures the rightmost wave emanating from the Riemann problem at the left face does not intersect with the right face, and vice versa. To determine the size of the time step Δt, we must look at the CFL coefficient, so that the time step is given by

$$\Delta t = \frac{C_{cfl}\Delta x}{S^n_{\max}}, \tag{4.1}$$

where C_{cfl} is the Courant or CFL coefficient which satisfies

$$0 < C_{cfl} \leq 1. \tag{4.2}$$

The time marching scheme is more efficient the close the coefficient C_{CFL} is to 1. $S^n_{\max}$ is the largest wave speed present throughout the domain at time level n [20]. The consequence of this is that no wave present in the solution of all Riemann problems travels more than a distance Δx in time Δt. For the time-dependent, one dimensional Euler equations, we can estimate $S^n_{\max}$ as

$$S^n_{\max} = \max_i \left\{ \left| S^L_{i+\frac{1}{2}} \right|, \left| S^R_{i+\frac{1}{2}} \right| \right\}, \tag{4.3}$$

for $i = 0, ..., M$, where $S^L_{i+\frac{1}{2}}$, $S^R_{i+\frac{1}{2}}$ are the wave speeds of the left and right non-linear waves present in the solution of the Riemann problem $R\left(\mathbf{U}^n_i, \mathbf{U}^n_{i+1}\right)$. The Riemann problem generates three waves; non-linear waves, which can be shocks or rarefactions and are the fastest waves. For rarefaction waves we select the speed of the head and for shock waves we select the shock speed. It is important to note that when sampling the wave speeds we must include the boundaries, as these may generate large wave speeds. By using (4.3) to find $S^n_{\max}$ and thus Δt of (4.1) we have a simple and reliable procedure [20].

4.3 Boundary Conditions

Boundary conditions are needed at the boundaries $x = 0$ and $x = L$ for a domain $[0, L]$ discretised into M computing cells of length Δx. In addition, the boundary conditions provide the numerical fluxes $\mathbf{F}_{\frac{1}{2}}$, and $\mathbf{F}_{M+\frac{1}{2}}$. We require these in order to apply the conservative formula (3.5) to update the extreme cells I_1 and I_M to the next time level $n + 1$, and they may result directly in $\mathbf{F}_{\frac{1}{2}}$ and $\mathbf{F}_{M+\frac{1}{2}}$. We can also force fictious data values in the fictious cells I_0 and I_{M+1}, adjacent to I_1 and I_M. By doing this, boundary Riemann problems are solved and the corresponding Godunov fluxes are computed [20].

We consider two types of boundary conditions in this study, *reflective* and *transparent* conditions.

4.3.1 Reflective boundaries

Reflective boundaries refer physically to walls at either side of the domain. We can think of it as a boundary $x = L$ then the physical situation is modelled creating a ficitious state $W_(M+1)^n$ to the right of the boundary and defining the boundary Riemann problem as $R(W_M^(n), W_(M+1)^n)$. This fictitious state is defined from the state W^n_M inside the computational domain, in other words

$$\rho^n_{M+1} = \rho^n_M, \; u^n_{M+1} = -u^n_M, \; p^n_{M+1} = p^n_M. \tag{4.4}$$

The exact solution of this depends on the value of u^n_M, if it is greater than zero the solution consists of two shock waves. If it is less than or equal to zero there are two rarefaction waves. For both scenarios $u_* = 0$ along the boundary which is the desired condition at the solid fixed impermeable boundary [20].

4.3.2 Transparent boundaries

The need to define finite, or infinitesimally small, computational domains gives rise to the transparent boundaries. These boundary conditions are a numerical attempt to provide boundaries that allow waves to pass through without having any effect on them. For the one dimensional case this objective is reasonably satisfied [20]. For a transmissive right boundary the conditions are

$$\rho_{M+1}^n = \rho_M^n,\ u_{M+1}^n = u_M^n,\ p_{M+1}^n = p_M^n. \tag{4.5}$$

This Riemann problem has the property that no wave of finite strength is produced at the boundary that may affect the flow inside the domain [20]. It is worth mentioning reminding ourselves at this point that we must remember to consider the wave speeds generated at the boundaries after the application of these boundary conditions when we select the time step size.

5 Approximate Riemann Solvers

These approximate Riemann solvers are introduced in chronological order.

5.1 Roe (1981)

The Roe solver, devised by Roe [12], is an approximate Riemann solver based around the Godunov scheme and works by looking for an estimate for the intercell numerical flux or Godunov flux $\mathbf{F}_{i+\frac{1}{2}}$ at the interface between two computational cells $\mathbf{U}_i$ and $\mathbf{U}_{i+\frac{1}{2}}$ on a discretised space-time computational domain.

5.1.1 The Original Roe Method

To determine the Godunov method we need to find the average eigenvalues $\tilde{\lambda}_i$, the corresponding averaged right eigenvectors $\tilde{\mathbf{K}}^{(i)}$ and averaged wave strengths $\tilde{\alpha}_i$. In the 1981 paper [12] an averaged Jacobian matrix $\tilde{\mathbf{A}}$, the Roe matrix, is found and from which $\tilde{\lambda}_i$, $\tilde{\mathbf{K}}^{(i)}$ and $\tilde{\alpha}_i$ follow. In the matrix $\tilde{\mathbf{A}}$ the properties (A)-(C) are enforced.
Property (A): Hyperbolicity of the system. $\tilde{\mathbf{A}}$ is required to have real eigenvalues $\tilde{\lambda}_i = \tilde{\lambda}_i(\mathbf{U}_{L,}\mathbf{U}_R)$, which we choose to order as

$$\tilde{\lambda}_1 \leqslant \tilde{\lambda}_2 \leqslant ... \leqslant \tilde{\lambda}_m \tag{5.1}$$

and a complete set of linearly independent right eigenvectors

$$\tilde{\mathbf{K}}^{(1)}, \tilde{\mathbf{K}}^{(2)}, ..., \tilde{\mathbf{K}}^{(m)}. \tag{5.2}$$

Property (B): Consistency with the exact Jacobian

$$\tilde{\mathbf{A}}(\mathbf{U}, \mathbf{U}) = \mathbf{A}(\mathbf{U}). \tag{5.3}$$

Property (C): Conservation across discontinuities

$$\mathbf{F}(\mathbf{U}_R) - \mathbf{F}(\mathbf{U}_L) = \tilde{\mathbf{A}}(\mathbf{U}_R - \mathbf{U}_L) \tag{5.4}$$

Property (C) is the crucial property, as it narrows choices for $\tilde{\mathbf{A}}$. Roe showed that the existence of a matrix $\tilde{\mathbf{A}}$ satisfying property (C) is assured by the mean value theorem [12]. To find the vector

$\tilde{\mathbf{A}}$, Roe introduced the idea of a *parameter vector* $\mathbf{Q}$, such that both the vector of conserved variables $\mathbf{U}$ and the flux vector $\mathbf{F}(\mathbf{U})$ could be expressed in terms of $\mathbf{Q}$. That is

$$\mathbf{U} = \mathbf{U}(\mathbf{Q}),\ \mathbf{F} = \mathbf{F}(\mathbf{Q}). \tag{5.5}$$

This is followed by two important steps. First the changes

$$\Delta\mathbf{U} = \mathbf{U}_R - \mathbf{U}_L,\ \Delta\mathbf{F} = \mathbf{F}(\mathbf{U}_R) - \mathbf{F}(\mathbf{U}_L) \tag{5.6}$$

can be expressed in terms of the change $\Delta\mathbf{Q} = \mathbf{Q}_R - \mathbf{Q}_L$. And secondly, averages are obtained in terms of *simple arithmetic means* of $\mathbf{Q}$. We now illustrate the technique as applied to the Euler equations in one dimension.

The Euler equations Here we present the Roe Riemann solver as applied to the Riemann problem for the x-split one dimensional time dependent Euler equations for ideal gases.

The exact x-direction Jacobian matrix $\mathbf{A}(\mathbf{U})$ is

$$\mathbf{A} = \begin{bmatrix} 0 & 1 & 0 \\ \tilde{\gamma}H - u^2 - a^2 & (3-\gamma)u & \tilde{\gamma} \\ \frac{1}{2}u\left[(\gamma-3)H - a^2\right] & H - \gamma u^2 & \gamma u \end{bmatrix}. \tag{5.7}$$

where $\tilde{\gamma} = \gamma - 1$. The eigenvalues are

$$\lambda_1 = u - a,\ \lambda_2 = \lambda_3 = \lambda_4 = u,\ \lambda_5 = u + a, \tag{5.8}$$

where $a = \sqrt{\gamma p/\rho}$ is the speed of sound. The corresponding right eigenvectors are

$$K^{(1)} = \begin{bmatrix} 1 \\ u - a \\ H - ua \end{bmatrix};K^{(2)} = \begin{bmatrix} 1 \\ u \\ \frac{1}{2}u^2 \end{bmatrix};K^{(3)} = \begin{bmatrix} 1 \\ u + a \\ H + ua \end{bmatrix}. \tag{5.9}$$

Where H is the total enthalpy

$$H = \frac{E + p}{\rho} \tag{5.10}$$

and E is the total energy per unit volume

$$E = \frac{1}{2}\rho u^2 + \rho e, \tag{5.11}$$

with e representing the specific internal energy, which for ideal gases is

$$e = \frac{p}{(\gamma - 1)\rho}. \tag{5.12}$$

Roe then chooses the *parameter vector*

$$\mathbf{Q} \equiv \begin{bmatrix} q_1 \\ q_2 \\ q_3 \end{bmatrix} \equiv \sqrt{\rho} \begin{bmatrix} 1 \\ u \\ H \end{bmatrix}, \tag{5.13}$$

in which every component u_i of $\mathbf{U}$ and every component f_i of $\mathbf{F}(\mathbf{U})$ in (**??**)-(**??**) is a quadratic in the components q_i of $\mathbf{Q}$. In other words, $u_1 = q_1^2$ and $f_1 = q_1 q_2$, and so on. In fact, the property is valid for the components of the $\mathbf{G}$ and $\mathbf{H}$ fluxes for the full three-dimensional Euler equations.

The jumps $\Delta\mathbf{U}$ and $\Delta\mathbf{F}$ can be expressed in terms of the jump $\Delta\mathbf{Q}$ via two matrices $\tilde{\mathbf{B}}$ and $\tilde{\mathbf{C}}$. Roe [12] gives the following expressions

$$\tilde{\mathbf{B}} = \begin{bmatrix} 2\tilde{q}_1 & 0 & 0 \\ \tilde{q}_2 & \tilde{q}_1 & 0 \\ \frac{\tilde{q}_3}{\gamma} & \frac{\gamma-1}{\gamma}\tilde{q}_2 & \frac{\tilde{q}_1}{\gamma} \end{bmatrix} \tag{5.14}$$

and

$$\tilde{\mathbf{C}} = \begin{bmatrix} \tilde{q}_2 & \tilde{q}_1 & 0 \\ \frac{\gamma-1}{\gamma}\tilde{q}_3 & \frac{\gamma-1}{\gamma}\tilde{q}_2 & \frac{\tilde{q}_1}{\gamma} \\ 0 & \tilde{q}_3 & \tilde{q}_2 \end{bmatrix}. \tag{5.15}$$

The Roe matrix is then given by

$$\tilde{\mathbf{A}} = \tilde{\mathbf{B}}\tilde{\mathbf{C}}^{-1}. \tag{5.16}$$

The eigenvalues of $\tilde{\mathbf{A}}$ are

$$\tilde{\lambda}_1 = \tilde{u} - \tilde{a},\ \tilde{\lambda}_2 = \tilde{\lambda}_3 = \tilde{\lambda}_4 = \tilde{u},\ \tilde{\lambda} = \tilde{u} + \tilde{a} \tag{5.17}$$

and the corresponding right eigenvectors are

$$\tilde{\mathbf{K}}^{(1)} = \begin{bmatrix} 1 \\ \tilde{u} - \tilde{a} \\ \tilde{H} - \tilde{u}\tilde{a} \end{bmatrix};\ \tilde{\mathbf{K}}^{(2)} = \begin{bmatrix} 1 \\ \tilde{u} \\ \frac{1}{2}\tilde{u}^2 \end{bmatrix};\ \tilde{\mathbf{K}}^{(3)} = \begin{bmatrix} 1 \\ \tilde{u} + \tilde{a} \\ \tilde{H} - \tilde{u}\tilde{a} \end{bmatrix}. \tag{5.18}$$

The symbol $\tilde{r}$ in (5.17), (5.18)denotes a Roe average for a variable r. The relevant averages are given as follows

$$\left.\begin{aligned} \tilde{u} &= \frac{\sqrt{\rho_L}u_L + \sqrt{\rho_R}u_R}{\sqrt{\rho_L} + \sqrt{\rho_R}}, \\ \tilde{H} &= \frac{\sqrt{\rho_L}H_L + \sqrt{\rho_R}H_R}{\sqrt{\rho_L} + \sqrt{\rho_R}}, \\ \tilde{a} &= (\gamma - 1)\left[\tilde{H} - \tfrac{1}{2}\tilde{u}^2\right]. \end{aligned}\right\} \tag{5.19}$$

To determine the Roe numerical flux $\mathbf{F}_{i+\frac{1}{2}}$ it is neccessary to have the wave strengths $\tilde{\alpha}_i$. These can be obtained by projecting the jump $\Delta\mathbf{U}$ onto the right, averaged eigenvectors (5.18), that is

$$\Delta\mathbf{U} = \sum_{i=1}^{5} \tilde{\alpha}_i \tilde{\mathbf{K}}^{(i)}. \tag{5.20}$$

The left hand side of this equation is known, they are the jumps in Δu_i in the conserved quantity u_i, that is

$$\Delta u_i = (u_i)_R - (u_i)_L.$$

Arranging the solution conveniently for computation, we arrive at

$$\left.\begin{aligned}\tilde{\alpha}_2 &= \frac{\gamma-1}{\tilde{a}^2}\left[\Delta u_1\left(\tilde{H}-\tilde{u}^2\right)+\tilde{u}\Delta u_2-\Delta u_3\right],\\ \tilde{\alpha}_1 &= \frac{1}{2\tilde{a}}\left[\Delta u_1\left(\tilde{u}+\tilde{a}\right)-\Delta u_2-\tilde{a}\tilde{\alpha}_2\right],\\ \tilde{\alpha}_3 &= \Delta u_1-\left(\tilde{\alpha}_1+\tilde{\alpha}_2\right),\end{aligned}\right\} \tag{5.21}$$

Toro summarises the above by putting it into an algorithm to compute the Roe numerical flux $\mathbf{F}_{i+\frac{1}{2}}$ in one-dimension [20]:

1. Compute the Roe average values for $\tilde{u}$, $\tilde{H}$ and $\tilde{a}$ according to (5.19).
2. Computer the averaged eigenvalues $\tilde{\lambda}_i$ according to (5.17)
3. Compute the averaged right eigenvectors $\tilde{\mathbf{K}}^{(i)}$ according to (5.18).
4. Compute the wave strengths $\tilde{\alpha}_i$ according to (5.20).
5. Use the above quantities to compute $\mathbf{F}_{i+\frac{1}{2}}$.

5.2 Harten, Lax and van Leer (1983)

This section will present the Harten, Lax and van Leer (HLL) [7] Riemann solver and the extended HLLC (C stands for Contact) solver as it is applied to the three-dimensional time dependent Euler equations.

To recall, we are concerned with solving the Initial Boundary Value Problem (IVBP) numerically

$$\left.\begin{aligned}&\text{PDEs}: \mathbf{U}_t+\mathbf{F}(\mathbf{U})_x=0,\\ &\text{ICs}: \mathbf{U}(x,0)=\mathbf{U}^{(0)}(x),\\ &\text{BCs}: \mathbf{U}(0,t)=\mathbf{U}_t(t),\ \mathbf{U}(L,t)=\mathbf{U}_t(t),\end{aligned}\right\} \tag{5.22}$$

in a domain $x_l \leqslant x \leqslant x_r$, making use of the explicit conservative formula

$$\mathbf{U}_i^{n+1} = \mathbf{U}_i^n + \frac{\Delta t}{\Delta x}\left[\mathbf{F}_{i-\frac{1}{2}} - \mathbf{F}_{i+\frac{1}{2}}\right]. \tag{5.23}$$

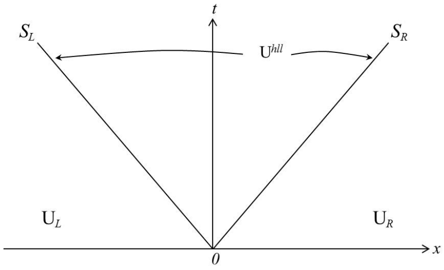

Figure 5.1: Approximate HLL Riemann solver. Solution in the *Star Region* consists of a single state $\mathbf{U}^{hll}$ separated from data states by two waves of speeds S_L and S_R

For a review of the Godunov method, we can refer back to Section 3. We recall the Godunov intercell numerical flux

$$\mathbf{F}_{i+\frac{1}{2}} = \mathbf{F}(\mathbf{U}_{i+\frac{1}{2}}(0)), \tag{5.24}$$

where $\mathbf{U}_{i+\frac{1}{2}}(0)$ is the exact similarity solution $\mathbf{U}_{i+\frac{1}{2}}(x/t)$ of the Rieman problem

$$\left.\begin{aligned} &\mathbf{U}_t + \mathbf{F}(\mathbf{U})_x = 0 \\ &\mathbf{U}(x,0) = \begin{cases} \mathbf{U}_L \; if \; x < 0, \\ \mathbf{U}_R \; if \; x > 0, \end{cases} \end{aligned}\right\} \tag{5.25}$$

evaluated at $x/t = 0$. The solver devised by Harten, Lax and van Leer [7] sets out to find direct approximations to the flux function $\mathbf{F}_{i+\frac{1}{2}}$. They put forward the following approximate Riemann solver

$$\tilde{\mathbf{U}}(x,t) = \begin{cases} \mathbf{U}_L \; if \; \frac{x}{t} \leqslant S_L, \\ \mathbf{U}^{hll} \; if \; S_L \leqslant \frac{x}{t} \leqslant S_R, \\ \mathbf{U}_R \; if \; \frac{x}{t} \geqslant S_R, \end{cases} \tag{5.26}$$

where $\mathbf{U}^{hll}$ is the constant state vector given by

$$\mathbf{U}^{hll} = \frac{S_R \mathbf{U}_R - S_L \mathbf{U}_L + F_L - F_R}{S_R - S_L}, \tag{5.27}$$

and the speeds S_L and S_R are known values. If we consider imaginary graph 5.1, which shows the structure of this approximate solution, we can see that it consists of three constant states separated by two waves. The *Star Region* consists of a *single* constant state; all intermediate states separated by intermediate waves are *lumped* into the single state $\mathbf{U}^{hll}$. It is important to make note that we do not take $\mathbf{F}^{hll} = \mathbf{F}(\mathbf{U}^{hll})$. The area of interest is the subsonic case $S_L \leqslant 0 \leqslant S_R$. Substituting $\mathbf{U}^{hll}$ in (5.27) yields

$$\mathbf{F}^{hll} = \mathbf{F}_L + S_L(\mathbf{U}^{hll} - \mathbf{U}_L), \tag{5.28}$$

or

$$\mathbf{F}^{hll} = \mathbf{F}_R + S_R(\mathbf{U}^{hll} - \mathbf{U}_R). \tag{5.29}$$

Use of (5.27) on (5.28) and (5.29) results in the HLL flux

$$\mathbf{F}^{hll} = \frac{S_R\mathbf{F}_L - S_L\mathbf{F}_R + S_L S_R(\mathbf{U}_R - \mathbf{U}_L)}{S_R - S_L}. \tag{5.30}$$

Which can be used to produce the corresponding intercell flux for the approximate Gudonov method

$$F^{hll}_{i+1} = \begin{cases} F_L \; if \; 0 \leqslant S_L, \\ \frac{S_R\mathbf{F}_L - S_L\mathbf{F}_R + S_L S_R(\mathbf{U}_R - \mathbf{U}_L)}{S_R - S_L}, \; if \; \mathrm{S_L} \leqslant 0 \leqslant \mathrm{S_R}, \\ F_R \; if \; 0 \geqslant S_R. \end{cases} \tag{5.31}$$

We will discuss the calculation of S_L and S_R after the discussion on the HLLC solver, in Section 5.2.2, but given those speeds we can use (5.31) in the conservative formula (5.23) to get an approximate Godunov method. In their paper, Harten, Lax and van Leer [7] showed that this Godunov scheme converges to the weak solution of conservation laws and proved that the converged solution is also the physical, entropy satisfying, solution of the conservation laws [20]. The requirements for this include that an approximate solution $\bar{\mathbf{U}}(x,t)$ is consistent with the integral form of the conservation laws if, when substituted for the exact solution $\mathbf{U}(x,t)$ in the Consistency Condition

$$\int_{x_L}^{x_R} \mathbf{U}(x,T)dx = x_R\mathbf{U}_R - x_L\mathbf{U}_L + T(\mathbf{F}_L - \mathbf{F}_R), \tag{5.32}$$

the right-hand side remains unaltered, that is, it has *consistency with the integral form of the conservation laws.*

One major flaw of the HLL scheme is exposed by contact discontinuities, shear waves and material interfaces. These waves are associated with the multiple eigenvalue $\lambda_2 = \lambda_3 = \lambda_4 = u$. In the integral

$$\frac{1}{T(S_R - S_L)} \int_{TS_L}^{TS_R} \mathbf{U}(x,T)dx = \frac{S_R\mathbf{U}_R - S_L\mathbf{U}_L + F_L - F_R}{S_R - S_L}, \tag{5.33}$$

the average across the wave structure is all that matters, without considering the spatial variations of the solution of the Riemann problem in the *Star Region.* In their paper, Harten, Law and van Leer [7] suggested this could be corrected by restoring the missing waves. Consequently, Toro, Spruce and Speares [19] proposed the HLLC scheme, where C stands for Contact. This scheme puts the middle waves back into the structure of the approximate Riemann solver.

5.2.1 The HLLC approximate Riemann solver

Considering 5.2, where the complete structure of the solution of the Riemann problem is contained in a sufficiently large control volume $[x_L, x_R] \times [0,T]$. We add now the middle speed S_* corre-

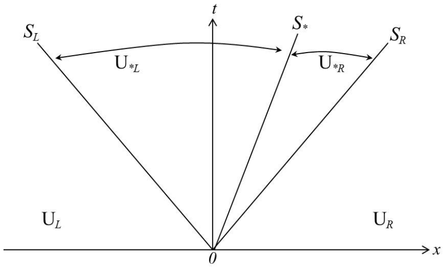

Figure 5.2: Approximate HLLC Riemann solver. Solution in the *Star Region* consists of two constant states separated by a middle wave speed of S_*.

sponding to the multiple eigenvalue $\lambda_2 = \lambda_3 = \lambda_4 = u$. The integral form of the conversation laws does not change from (5.33) even with variations of the integrand across S_*. With this addition, the consistency condition 5.32 becomes effectively the condition (5.33), and thus by splitting the left-hand side of (5.33) into two terms we obtain

$$\begin{aligned}\tfrac{1}{T(S_R-S_L)}\int_{TS_L}^{TS_R}\mathbf{U}(x,T)dx =& \tfrac{1}{T(S_R-S_L)}\int_{TS_L}^{TS_*}\mathbf{U}(x,T)dx \\ &+\tfrac{1}{T(S_R-S_L)}\int_{TS_*}^{TS_R}\mathbf{U}(x,T)dx\end{aligned} \tag{5.34}$$

And the integral averages are defined as

$$\left.\begin{aligned}\mathbf{U}_{*L} &= \tfrac{1}{T(S_R-S_L)}\int_{T_{SL}}^{T_{S*}}\mathbf{U}(x,T)dx,\\ \mathbf{U}_{*R} &= \tfrac{1}{T(S_R-S_L)}\int_{T_{S*}}^{T_{SR}}\mathbf{U}(x,T)dx.\end{aligned}\right\} \tag{5.35}$$

Substituting (5.35) into (5.34) and using (5.33), The Consistency Condition (5.32) becomes

$$\left(\frac{S_*-S_L}{S_R-S_L}\right)\mathbf{U}_{*L} + \left(\frac{S_R-S_*}{S_R-S_L}\right)\mathbf{U}_{*R} = \mathbf{U}^{hll}, \tag{5.36}$$

where $\mathbf{U}^{hll}$ is given by (5.27). Thus the HLLC approximate Riemann solver is given as follows

$$\tilde{\mathbf{U}}(x,t) = \begin{cases}\mathbf{U}_L \ if \ \frac{x}{t} \leqslant S_L,\\ \mathbf{U}_{*L} \ if \ S_L \leqslant \frac{x}{t} \leqslant S_*,\\ \mathbf{U}_{*R} \ if \ S_* \leqslant \frac{x}{t} \leqslant S_R,\\ \mathbf{U}_R \ if \ \frac{x}{t} \geqslant S_R.\end{cases} \tag{5.37}$$

And by integrating over appropriate control volumes, we obtain

$$\mathbf{F}_{*L} = \mathbf{F}_L + \mathbf{S}_L(\mathbf{U}_{*L} - \mathbf{U}_L), \tag{5.38}$$

$$\mathbf{F}_{*R} = \mathbf{F}_{*L} + \mathbf{S}_*(\mathbf{U}_{*R} - \mathbf{U}_{*L}), \tag{5.39}$$

$$\mathbf{F}_{*R} = \mathbf{F}_R + \mathbf{S}_R(\mathbf{U}_{*R} - \mathbf{U}_R). \tag{5.40}$$

Equations (5.38) - (5.40) are for the four unknown vectors $\mathbf{U}_{*L}$, $\mathbf{F}_{*L}$, $\mathbf{U}_{*R}$ and $\mathbf{F}_{*R}$. We can compare these to the HLL scheme equations (5.28) - (5.29), and substituting $\mathbf{F}_{*L}$ from 5.38 and $\mathbf{F}_{*R}$ from (5.40) into (5.39) gives the Consistency Condition (5.36) showing that these three equations are sufficient for ensuring consistency. In order to determine the fluxes $\mathbf{F}_{*L}$ and $\mathbf{F}_{*R}$ from 5.38 and 5.40 it is necessary to find the vectors $\mathbf{U}_{*L}$ and $\mathbf{U}_{*R}$ to make this possible. First we impose some conditions on the approximate Riemann solver

$$\left.\begin{aligned} &u_{*L} = u_{*R} = u_*, \\ &p_{*L} = p_{*R} = p_*, \\ &v_{*L} = v_L,\; v_{*R} = v_R, \\ &w_{*L} = W_L,\; w_{*R} = w_R, \end{aligned}\right\} \tag{5.41}$$

which are satisfied by the exact solution, and we can also set

$$S_* = u_* \tag{5.42}$$

And we can then rearrange (5.38) and (5.40) as

$$S_L\mathbf{U}_{*L} - \mathbf{F}_{*L} = \mathbf{Q}_L, \tag{5.43}$$

$$S_R\mathbf{U}_{*R} - \mathbf{F}_{*R} = \mathbf{Q}_R, \tag{5.44}$$

where $\mathbf{Q}_L$ and $\mathbf{Q}_R$ are known constant vectors. Using the conditions (5.41) - (5.42) in the above gives

$$U_{*K} = \rho_K\left(\frac{S_K - u_K}{S_K - S_*}\right)\begin{bmatrix} 1 \\ S_* \\ v_K \\ w_K \\ \frac{E_K}{\rho_K} + (S_* - u_K)\left[S_* + \frac{p_K}{\rho_K(S_K - U_K)}\right] \end{bmatrix}, \tag{5.45}$$

for $K = L$ and $K = R$. Thus the fluxes are completely determined. The HLLC flux for the approximate Godunov method can now be written as

$$\mathbf{F}^{hllc}_{i+\frac{1}{2}} = \begin{cases} \mathbf{F}_L \; if \; 0 \leqslant S_L, \\ \mathbf{F}_{*L} = \mathbf{F}_L + S_L(\mathbf{U}_{*L} - \mathbf{U}_L) \; if \; S_L \leqslant 0 \leqslant S_*, \\ \mathbf{F}_{*R} = \mathbf{F}_R + S_R(\mathbf{U}_{*R} - \mathbf{U}_R) \; if \; S_* \leqslant 0 \leqslant S_R, \\ \mathbf{F}_R \; if \; 0 \geqslant S_R. \end{cases} \tag{5.46}$$

where $\mathbf{U}_{*L}$ and $\mathbf{U}_{*R}$ are given by (5.45).

5.2.2 Wave-speed estimates

To allow for the calculation of the fluxes in both the HLL and HLLC schemes it is necessary to have algorithms for computing wave speeds. We just require speeds S_L and S_R for the HLL scheme, but require the additional middle wave speed S_* for the HLLC scheme. We will look at two ways of estimating S_L, S_R and S_*: direct estimates and pressure-velocity estimates.

Direct wave speed estimates The direct wave speed estimates are the most simple methods providing minimum and maximum signal velocities. The most simple of these is provided by Davis [2]

$$S_L = u_L - a_L,\ S_R = u_R + a_R \tag{5.47}$$

and

$$S_L = \min\left\{u_L - a_L, u_R - a_R\right\},\ S_R = \max\left\{u_R + a_R, u_R + a_R\right\}. \tag{5.48}$$

Because of the simplicity of these estimates, it is necessary to look at more complex estimates. We can also make use of the Roe [11] average eigenvalues, that we use in the Roe Riemann scheme, for the left and right non-linear waves

$$S_L = \tilde{u} - \tilde{a},\ S_R = \tilde{u} + \tilde{a}, \tag{5.49}$$

where $\tilde{u}$ and $\tilde{a}$ are the Roe-average particle and sound speeds respectively, given as

$$\tilde{u} = \frac{\sqrt{\rho_L}u_L + \sqrt{\rho_R}u_R}{\sqrt{\rho_L} + \sqrt{\rho_R}},\ \tilde{a} = \left[(\gamma - 1)\left(\tilde{H} - \frac{1}{2}\tilde{u}^2\right)\right]^{\frac{1}{2}}, \tag{5.50}$$

with the enthalpy $H = (E + p)/\rho$ approximated as

$$\tilde{H} = \frac{\sqrt{\rho_L}H_L + \sqrt{\rho_R}H_R}{\sqrt{\rho_L} + \sqrt{\rho_R}}. \tag{5.51}$$

More information about the Roe solver and scheme are given in the previous chapter. The Rusanov flux can be obtained by, is taking a positive speed S^+, setting $S_L = -S^+$ and $S_R = S^+$ in the HLL flux (refeq:10.21), as observed by Davis [14]

$$\mathbf{F}_{i+1/2} = \frac{1}{2}(\mathbf{F}_L + \mathbf{F}_R) - \frac{1}{2}S^+(\mathbf{U}_R - \mathbf{U}_L). \tag{5.52}$$

Its necessary to choose a speed S^+, Davis [2] considered

$$S^+ = \max\left\{|u_L - a_L, |u_R - a_R|, |u_L + a_L|, |u_R + a_R||\right\}, \tag{5.53}$$

which is bounded by [20]

.

$$S^{+} = \max\left\{|u_L| + a_L, |u_R| + a_R\right\}. \tag{5.54}$$

Both are considered and investigated in Section 7. Finally we consider the Einfeldt eigenvalues [4], which are motivated by the Roe values

$$S_L = \tilde{u} - \tilde{d},\ S_R = \tilde{u} + \tilde{d}, \tag{5.55}$$

where

$$\tilde{d}^2 = \frac{\sqrt{\rho_L}a_L^2 + \sqrt{\rho_R}a_R^2}{\sqrt{\rho_L} + \sqrt{\rho_R}} + \eta_2(u_R - u_L)^2 \tag{5.56}$$

and

$$\eta_2 = \frac{1}{2}\frac{\sqrt{\rho_L}\sqrt{\rho_R}}{\left(\sqrt{\rho_L} + \sqrt{\rho_R}\right)^2}. \tag{5.57}$$

Comparisons of the results given by these various wave speeds can be seen in (the following section).

Pressure-velocity based wave speed estimates Finding wave speed estimates by estimating the pressure p_* in the *Star Region* was first proposed by Toro et. al. [19]. Since for the HLLC scheme we also require S_*, the P-V estimate is the sensible choice, although in Section 7 we apply it to both HLL and HLLC schemes. Two possible ways of doing this include finding an estimate for the particle velocity u_* and the second derives S_* from the estimates S_L and S_R using conditions (5.41) in equations (5.43) - (5.44) (see [1]). Assuming we have estimates for p_* and u_*, then we choose the following wave speeds

$$S_L = u_L - a_L q_L,\ S_* = u_*,\ S_R = u_R + a_R q_R, \tag{5.58}$$

where

$$q_K = \begin{cases} 1\ if\ p_* \leqslant p_K \\ \left[1 + \frac{\gamma+1}{2\gamma}\left(p_*/p_K - 1\right)\right]^{\frac{1}{2}}\ if\ p_* > p_K. \end{cases} \tag{5.59}$$

This choice of wave speeds discriminates between shock and rarefaction waves. If the K wave ($K = L$ or $K = R$) is a rarefaction then the speed S_K corresponds to the characteristic speed of the head of the rarefaction, which carries the fastest signal. If the wave is a shock wave then the speed corresponds to an approximation of the true shock speed; the wave relations used are exact but the pressure ratio across the shock is approximated, because the solution for p_* is an approximation. The Primitive Variable Riemann Solvers approximate Riemann solver [17] gives

$$p_{pv} = \frac{1}{2}(p_L + p_R) - \frac{1}{2}(u_R - u_L)\bar{\rho}\bar{a},\ u_{pv} = \frac{1}{2}(u_L + u_R) - \frac{1}{2}\frac{(p_R - p_L)}{\bar{\rho}\bar{a}}, \tag{5.60}$$

where

$$\bar{\rho} = \frac{1}{2}(\rho_L + \rho_R),\ \bar{a} = \frac{1}{2}(a_L + a_R). \tag{5.61}$$

The approximations given in 5.60 and 5.61 can be used in (5.58) - (5.59) to obtain wave speed estimates for the HLL and HLLC schemes. There are other ways to approximate p_* and u_*, such as the Two-Rarefaction Riemann solver, but due to time restraints these were not investigated (see Toro sect 9.4.1).

5.3 Osher-Solomon (1982)

The final scheme being considered in this study is the Osher-Solomon scheme, devised as an upwind finite difference approximation to systems of nonlinear hyperbolic conservation laws [9]. It is an attractive scheme due to the smoothness of the numerical flux; proving to be entropy satisfying and in practical computations it is seen to handle the sonic flow well [20]. This chapter will look at how to apply the Osher-Solomon method to nonlinear hyperbolic conservation laws, looking specifically at the Euler equations, and will describe the two-different methods of ordering the flux for computation.

5.3.1 Osher-Solomon for the Euler equations

In this section we take the time-dependent Euler equations and develop the Osher-Solomon scheme for them, with both P and O orderings. We consider first the one-dimensional case

$$\mathbf{U}_t + \mathbf{F}(\mathbf{U})_x = 0 \tag{5.62}$$

$$\mathbf{U} = \begin{bmatrix} \rho \\ \rho u \\ E \end{bmatrix}, \ \mathbf{F}(\mathbf{U}) = \begin{bmatrix} \rho u \\ \rho u^2 + p \\ u(E+p) \end{bmatrix}. \tag{5.63}$$

Where we have considered the details of these equations in Chapter 2. The explicit conservative formula requires us to have an expression for the intercell flux $\mathbf{F}_{i+\frac{1}{2}}$

$$\mathbf{U}_i^{n+1} = \mathbf{U}_i^n + \frac{\Delta t}{\Delta x}\left[\mathbf{F}_{i-\frac{1}{2}} - \mathbf{F}_{i+\frac{1}{2}}\right]. \tag{5.64}$$

And we can recall that the Jacobian atrix $\mathbf{A}(\mathbf{U})$ has eigenvalues

$$\lambda_1 = u - 1, \ \lambda_2 = u, \ \lambda_3 = u + a \tag{5.65}$$

and right eigenvectors

$$\mathbf{K}^{(1)} = \begin{bmatrix} 1 \\ u - a \\ H - ua \end{bmatrix}, \ \mathbf{K}^{(2)} = \begin{bmatrix} 1 \\ u \\ \frac{1}{2}u^2 \end{bmatrix}, \ \mathbf{K}^{(3)} = \begin{bmatrix} 1 \\ u + a \\ H + ua \end{bmatrix}. \tag{5.66}$$

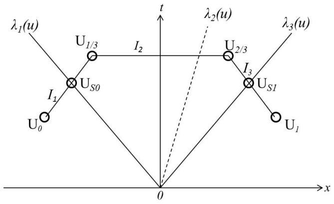

Figure 5.3: Possible configuration of integration paths $I_k(\mathbf{U})$, intersection points $\mathbf{U}_{\frac{1}{3}}$, $\mathbf{U}_{\frac{2}{3}}$ and sonic points $\mathbf{U}_{S0}$, $\mathbf{U}_{S1}$ in physical space $x - t$ for a 3 by 3 system

5.3 shows the structure of the solution of the Riemann problem with data $\mathbf{U}_0$, $\mathbf{U}_1$ in the $x - t$ plane. We see also the partial integration paths $I_1(\mathbf{U})$, $I_2(\mathbf{U})$, $I_3(\mathbf{U})$, the intersection points $\mathbf{U}_{\frac{1}{3}}$, $\mathbf{U}_{\frac{2}{3}}$ and the sonic points $\mathbf{U}_{S0}$, $\mathbf{U}_{S1}$ in phase space; which follow the *P-ordering*. To obtain the Osher-Solomon flux formulae we can look at the problem in two steps. The first step finds the intersection points $\mathbf{U}_{\frac{1}{3}}$ and $\mathbf{U}_{\frac{2}{3}}$, which are then identified with the states $\mathbf{U}_{*L}$ and $\mathbf{U}_{*R}$ in the solution of the Riemann problem. The second step involves evaluating the integrals around the integration paths to obtain the intercell flux.

P-ordering The P in *P-ordering* stands for physical ordering of the integration paths for the Euler equations, as shown in 5.3. We can see from the figure that the states $\mathbf{U}_0$ and $\mathbf{U}_{\frac{1}{3}}$ are connected by the partial integration path $I_1(\mathbf{U})$, which is taken as tangential to the right eigenvector $\mathbf{K}_{(1)}(\mathbf{U})$ in (5.66). Likewise, $I_2(\mathbf{U})$ connects $\mathbf{U}_{\frac{1}{3}}$ to $\mathbf{U}_{\frac{2}{3}}$ and $I_3(\mathbf{U})$ connects $\mathbf{U}_{\frac{2}{3}}$ to $\mathbf{U}_1$. In order to obtain the intersection and sonic points the physically correct Generalised Riemann Invariants are invoked (see Section 3.1.3 of [20]).

Intersection and Sonic Points. In order to find $\mathbf{U}_{\frac{1}{3}}$ and $\mathbf{U}_{\frac{2}{3}}$ we use the Generalised Riemann Invariants

$$I_L \equiv u + \frac{2a}{\gamma - 1} = \text{constant} \tag{5.67}$$

$$I_R \equiv u - \frac{2a}{\gamma - 1} = \text{constant} \tag{5.68}$$

to relate $\mathbf{U}_0$ to $\mathbf{U}_{\frac{1}{3}}$ and $\mathbf{U}_{\frac{2}{3}}$ to $\mathbf{U}_1$. If the left and right nonlinear waves are rarefaction waves then (5.67) - (5.68) are exact relations. These waves can either be shock or rarefactions and so the intersection points $\mathbf{U}_{\frac{1}{3}}$ and $\mathbf{U}_{\frac{2}{3}}$ are approximations [20]. The underlying assumption here though is that both nonlinear waves are rarefaction which corresponds to the Two-Rarefaction approximation TRRS (see [20] section 9.4.1). By using (5.67) across the left wave we get

$$u_* + \frac{2a_{\frac{1}{3}}}{\gamma - 1} = u_0 + \frac{2a_0}{\gamma - 1} \tag{5.69}$$

and similarly using (5.68) across the right wave

$$u_* - \frac{2a_{\frac{2}{3}}}{\gamma - 1} = u_1 - \frac{2a_1}{\gamma - 1} \tag{5.70}$$

where u_* is the common particle velocity for $\mathbf{U}_{\frac{1}{3}}$ and $\mathbf{U}_{\frac{2}{3}}$. We also know that the pressure p_* is also common

$$u_{\frac{1}{3}} = u_{\frac{2}{3}} = u_* = \text{constant},\ p_{\frac{1}{3}} = p_{\frac{2}{3}} = p_* = \text{constant}. \tag{5.71}$$

Applying the isentropic law, that entropy is constant, to the left and right waves gives

$$a_{\frac{1}{3}} = a_0(p_*/p_0)^z,\ a_{\frac{2}{3}} = a_1(p_*/p_1)^z, \tag{5.72}$$

with

$$z = \frac{\gamma - 1}{2\gamma}. \tag{5.73}$$

Using (5.69) and (5.72) we get

$$u_* = u_0 - \frac{2a_0}{\gamma - 1}\left[\left(\frac{p_*}{p_0}\right)^z - 1\right]. \tag{5.74}$$

And by using (5.70) and (5.72)

$$u_* = u_1 + \frac{2a_1}{\gamma - 1}\left[\left(\frac{p_*}{p_1}\right)^z - 1\right]. \tag{5.75}$$

Solving for p_* and u_* we obtain

$$p_* = \left[\frac{a_0 + a_1 - (u_1 - u_0)(\gamma - 1)/2}{a_0/p_0^z + a_1/p_1^z}\right]^{\frac{1}{z}}, \tag{5.76}$$

$$u_* = \frac{Hu_0/a_0 + u_1/a_1 + 2(H-1)(\gamma - 1)}{H/a_0 + 1/a_1}, \tag{5.77}$$

with

$$H = (p_0/p_1)^z.$$

The values for the densities $\rho_{\frac{1}{3}}$ and $\rho_{\frac{2}{3}}$ equate to

$$\rho_{\frac{1}{3}} = \rho_0\left(\frac{p_*}{p_0}\right)^{\frac{1}{\gamma}},\ \rho_{\frac{2}{3}} = \rho_1\left(\frac{p_*}{p_1}\right)^{\frac{1}{\gamma}}. \tag{5.78}$$

And thus the complete solution for $\mathbf{U}_{\frac{1}{3}}$, $\mathbf{U}_{\frac{2}{3}}$ is given by (5.76) - (5.78). In order to compute the sonic points $\mathbf{U}_{S0}$ and $\mathbf{U}_{S1}$ we first enforce the sonic conditions $\lambda_1 = u - a = 0$ and $\lambda_3 = u + a = 0$

and then by applying the Generalised Riemann Invariants [20]. The solution for the left sonic point becomes

$$\left.\begin{aligned} &u_{S0} = \tfrac{\gamma-1}{\gamma+1}u_0 + \tfrac{2a_0}{\gamma+1},\ a_{S0} = u_{S0}, \\ &\rho_{S0} = \rho_0\Big(\tfrac{a_{S0}}{a_0}\Big)^{\frac{2}{\gamma-1}},\ p_{S0} = p_0\Big(\tfrac{\rho_{S0}}{\rho_0}\Big)^{\gamma}. \end{aligned}\right\} \tag{5.79}$$

Similarly, for the right sonic point

$$\left.\begin{aligned} &u_{S1} = \tfrac{\gamma-1}{\gamma+1}u_1 - \tfrac{2a_1}{\gamma+1},\ a_{S1} = -u_{S1}, \\ &\rho_{S1} = \rho_1\Big(\tfrac{a_{S1}}{a_1}\Big)^{\frac{2}{\gamma-1}},\ p_{S1} = p_1\Big(\tfrac{\rho_{S1}}{\rho_1}\Big)^{\gamma}. \end{aligned}\right\} \tag{5.80}$$

Integration along partial paths. For the Osher-Solomon intercell flux we use

$$\mathbf{F}_{i+\frac{1}{2}} = \mathbf{F}_0 + \int_{\mathbf{U}_0}^{\mathbf{U}_1} \mathbf{A}^-(\mathbf{U})d\mathbf{U},$$

where the integral in phase space along the path

$$I(\mathbf{U}) = I_1(\mathbf{U}) \cup I_2(\mathbf{U}) \cup I_3(\mathbf{U})$$

gives

$$\mathbf{F}_{i+\frac{1}{2}} = \mathbf{F}_0 + \int_{\mathbf{U}_0}^{\mathbf{U}_{\frac{1}{3}}} \mathbf{A}^-(\mathbf{U})d\mathbf{U} + \int_{\mathbf{U}_{\frac{1}{3}}}^{\mathbf{U}_{\frac{2}{3}}} \mathbf{A}^-(\mathbf{U})d\mathbf{U} + \int_{\mathbf{U}_{\frac{2}{3}}}^{\mathbf{U}_1} \mathbf{A}^-(\mathbf{U})d\mathbf{U}. \tag{5.81}$$

For brevity the integration results are not given but the 16 realisable results given from integration have been tabulated in (5.1), more information on the results given by (5.81) can be found in Section 12.3.1 of [20].

	$u_0 - a_0 \geqslant 0$ $u_1 + a_1 \geqslant 0$	$u_0 - a_0 \geqslant 0$ $u_1 + a_1 \leqslant 0$	$u_0 - a_0 \leqslant 0$ $u_1 + a_1 \geqslant 0$	$u_0 - a_0 \leqslant 0$ $u_1 + a_1 \leqslant 0$
$u_* \geqslant 0,\ u_* - a_{\frac{1}{3}} \geqslant 0$	$\mathbf{F}_0$	$\mathbf{F}_0 + \mathbf{F}_1 + \mathbf{F}_{S1}$	$\mathbf{F}_{S1}$	$\mathbf{F}_{S0} - \mathbf{F}_{S1} + \mathbf{F}_1$
$u_* \geqslant 0,\ u_* - a_{\frac{1}{3}} \leqslant 0$	$\mathbf{F}_0 - \mathbf{F}_{S0} + \mathbf{F}_{\frac{1}{3}}$	$\mathbf{F}_0 - \mathbf{F}_{S0} + \mathbf{F}_{\frac{1}{3}} - \mathbf{F}_{S1} + \mathbf{F}_1$	$\mathbf{F}_{\frac{1}{3}}$	$\mathbf{F}_1 + \mathbf{F}_{\frac{1}{3}} - \mathbf{F}_{S1}$
$u_* \leqslant 0,\ u_* + a_{\frac{2}{3}} \geqslant 0$	$\mathbf{F}_0 - \mathbf{F}_{S0} + \mathbf{F}_{\frac{2}{3}}$	$\mathbf{F}_0 - \mathbf{F}_{S0} + \mathbf{F}_{\frac{2}{3}} - \mathbf{F}_{S1} + \mathbf{F}_1$	$\mathbf{F}_{\frac{2}{3}}$	$\mathrm{F}_{\frac{2}{3}} + \mathbf{F}_{S1} - \mathbf{F}_1$
$u_* \leqslant 0,\ u_* + a_{\frac{2}{3}} \leqslant 0$	$\mathbf{F}_0 - \mathbf{F}_{S0} + \mathbf{F}_{S1}$	$\mathbf{F}_0 - \mathbf{F}_{S0} + \mathbf{F}_1$	F_{S1}	$\mathbf{F}_1$

Table 5.1: Osher-Solomon flux formulae for the Euler equations using P-ordering of the integration paths, $\mathbf{F}_k = \mathbf{F}(\mathbf{U}_k)$ [20]

O-ordering The *O-ordering* of integration paths is the exact opposite of the *P-ordering* method described in the previous section. We can first illustrate the *O-ordering* applied to a 3 x 3 system, see 5.3, like the Euler equations. The *O-ordering* method can be seen like assigning the eigenvalue $\lambda_3(\mathbf{U})$ and eigenvector $\mathbf{K}^{(1)}(\mathbf{U})$ to the wave family with eigenvalue $\lambda_1(\mathbf{U})$ and eigenvector $\mathbf{K}^{(3)}(\mathbf{U})$, and vice-versa.

Intersection and sonic points. Similar to the *P-ordering* technique, we determine the intersection points $\mathbf{U}_{\frac{1}{3}}$ and $\mathbf{U}_{\frac{2}{3}}$ by using the Generalised Riemann Invariants. The main difference is that $\mathbf{U}_0$ and $\mathbf{U}_{\frac{1}{3}}$ are connected using the *right* Riemann Invariant and $\mathbf{U}_{\frac{2}{3}}$ is connected to $\mathbf{U}_1$ using the left. Therefore we have

$$I_L \equiv u_* + \frac{2a_{\frac{1}{3}}}{\gamma - 1} = u_0 - \frac{2a_0}{\gamma - 1} \tag{5.82}$$

$$I_R \equiv u_* - \frac{2a_{\frac{2}{3}}}{\gamma - 1} = u_1 + \frac{2a_1}{\gamma - 1} \tag{5.83}$$

Similarly we take u_* and p_* to be common particle velocity and pressure at points $\mathbf{U}_{\frac{1}{3}}$ and $\mathbf{U}_{\frac{2}{3}}$. Using (5.72) in (5.82) we get

$$u_* = u_0 + \frac{2a_0}{\gamma - 1}\left[\left(\frac{p_*}{p_0}\right)^z - 1\right]. \tag{5.84}$$

and using (5.72) in (5.83) we get

$$u_* = u_1 - \frac{2a_1}{\gamma - 1}\left[\left(\frac{p_*}{p_1}\right)^z - 1\right]. \tag{5.85}$$

Solving for p_* we get

$$p_* = \left[\frac{a_0 + a_1 - (u_1 - u_0)(\gamma - 1)/2}{a_0/p_0^z + a_1/p_1^z}\right]^{\frac{1}{z}}. \tag{5.86}$$

It is possible to rearrange (5.84) and (5.85) to get

$$p_* = p_0\left[\frac{\gamma - 1}{2a_0}(u_* - u_0) + 1\right]^{\frac{1}{z}}, \tag{5.87}$$

$$p_* = p_1\left[\frac{\gamma - 1}{2a_1}(u_1 - u_*) + 1\right]^{\frac{1}{z}}, \tag{5.88}$$

so the solution for u_* is given as

$$u_* = \frac{Hu_0/a_0 + u_1/a_1 + 2(H-1)(\gamma - 1)}{H/a_0 + 1/a_1}, \tag{5.89}$$

with H and z as defined in *P-ordering*. Envoking the isentropic law again, we can find solutions for $\rho_{\frac{1}{3}}$ and $\rho_{\frac{2}{3}}$

$$\rho_{\frac{1}{3}} = \rho_0\left(\frac{p_*}{p_0}\right)^{\frac{1}{\gamma}}, \ \rho_{\frac{2}{3}} = \rho_1\left(\frac{p_*}{p_1}\right)^{\frac{1}{\gamma}}. \tag{5.90}$$

Next, we find the sonic points $\mathbf{U}_{S0}$ and $\mathbf{U}_{S1}$ by first connecting $\mathbf{U}_0$ and $\mathbf{U}_{\frac{1}{3}}$ via the *right* Riemann Invariant

$$u_{S0} = \frac{2a_{S0}}{\gamma - 1} + u_0 - \frac{2a_0}{\gamma - 1}.$$

Then we enforce the sonic condition to obtain

$$\lambda_3(\mathbf{U}) = u_{S0} + a_{S0} = 0$$

along $I_3(\mathbf{U})$ and applying the isentropic law we obtain the solution

$$\left.\begin{array}{l} u_{S0} = \frac{\gamma-1}{\gamma+1} u_0 - \frac{2a_0}{\gamma+1},\ a_{S0} = -u_{S0}, \\ \rho_{S0} = \rho_0 \left(\frac{a_{S0}}{a_0}\right)^{\frac{2}{\gamma-1}},\ p_{S0} = p_0 \left(\frac{\rho_{S0}}{\rho_0}\right)^{\gamma}. \end{array}\right\} \tag{5.91}$$

The solution for the right sonic point $\mathbf{U}_{S1}$ is

$$\left.\begin{array}{l} u_{S1} = \frac{\gamma-1}{\gamma+1} u_1 + \frac{2a_1}{\gamma+1},\ a_{S1} = u_{S1}, \\ \rho_{S1} = \rho_1 \left(\frac{a_{S1}}{a_1}\right)^{\frac{2}{\gamma-1}},\ p_{S1} = p_1 \left(\frac{\rho_{S1}}{\rho_1}\right)^{\gamma}. \end{array}\right\} \tag{5.92}$$

Integration along partial paths. To compute the Osher-Solomon intercell flux

$$\mathbf{F}_{i+\frac{1}{2}} = \mathbf{F}_0 + \int_{\mathbf{U}_0}^{\mathbf{U}_1} \mathbf{A}^-(\mathbf{U}) d\mathbf{U}, \tag{5.93}$$

we need to obtain

$$\int_{\mathbf{U}_0}^{\mathbf{U}_1)} \mathbf{A}^-(\mathbf{U})d\mathbf{U} = \int_{\mathbf{U}_0}^{\mathbf{U}_{\frac{1}{3}}} \mathbf{A}^-(\mathbf{U})d\mathbf{U} + \int_{\mathbf{U}_{\frac{1}{3}}}^{\mathbf{U}_{\frac{2}{3}}} \mathbf{A}^-(\mathbf{U})d\mathbf{U} + \int_{\mathbf{U}_{\frac{2}{3}}}^{\mathbf{U}_1} \mathbf{A}^-(\mathbf{U})d\mathbf{U}. \tag{5.94}$$

By using *O-ordering* we obtain

$$\int_{\mathbf{U}_0}^{\mathbf{U}_{\frac{1}{3}}} \mathbf{A}^-(\mathbf{U})d\mathbf{U} = \int_{I_3(\mathbf{U})} \mathbf{A}^-(\mathbf{U})d\mathbf{U}, \tag{5.95}$$

$$\int_{\mathbf{U}_{\frac{1}{3}}}^{\mathbf{U}_{\frac{2}{3}}} \mathbf{A}^-(\mathbf{U})d\mathbf{U} = \int_{I_2(\mathbf{U})} \mathbf{A}^-(\mathbf{U})d\mathbf{U}, \tag{5.96}$$

$$\int_{\mathbf{U}_{\frac{2}{3}}}^{\mathbf{U}_1} \mathbf{A}^-(\mathbf{U})d\mathbf{U} = \int_{I_1(\mathbf{U})} \mathbf{A}^-(\mathbf{U})d\mathbf{U}. \tag{5.97}$$

Tables of evaluations of these are beyond the scope of this project, but for further details see section 12.3.2 of [20]. A table of realisable combinations is given in (5.2), which is what will be called on later in this work.

	$u_0 + a_0 \geqslant 0$ $u_1 + a_1 \geqslant 0$	$\mathrm{u}_0 + a_0 \geqslant 0$ $\mathrm{u}_1 - a_1 \leqslant 0$	$\mathrm{u}_0 + a_0 \leqslant 0$ $\mathrm{u}_1 - a_1 \geqslant 0$	$\mathrm{u}_0 + a_0 \leqslant 0$ $\mathrm{u}_1 + a_1 \leqslant 0$
$u_* + a_{\frac{1}{3}} \leqslant 0$	$\mathrm{F}_0 - \mathbf{F}_{S0} + \mathbf{F}_{S1}$	$\mathrm{F}_0 - \mathbf{F}_{S0} + \mathbf{F}_1$	F_{S1}	F_1
$u_* + a_{\frac{1}{3}} \geqslant 0,\ u_* \leqslant 0$	$\mathrm{F}_0 - \mathbf{F}_{\frac{1}{3}} + \mathbf{F}_{S1}$	$\mathrm{F}_0 - \mathbf{F}_{\frac{1}{3}} + \mathbf{F}_1$	$\mathrm{F}_{S0} - \mathbf{F}_{\frac{1}{3}} + \mathbf{F}_{S1}$	$\mathrm{F}_{S0} - \mathbf{F}_{\frac{1}{3}} + \mathbf{F}_1$
$u_* - a_{\frac{2}{3}} \geqslant 0$	F_0	$\mathrm{F}_0 - \mathbf{F}_{S1} + \mathbf{F}_1$	F_{S0}	$\mathrm{F}_{S0} - \mathbf{F}_{S1} + \mathbf{F}_1$
$u_* - a_{\frac{2}{3}} \leqslant 0,\ u_* \geqslant 0$	$\mathrm{F}_0 - \mathbf{F}_{\frac{2}{3}} + \mathbf{F}_{S1}$	$\mathrm{F}_0 - \mathbf{F}_{\frac{2}{3}} + \mathbf{F}_1$	$\mathrm{F}_{S0} - \mathbf{F}_{\frac{2}{3}} + \mathbf{F}_{S1}$	$\mathrm{F}_{S0} - \mathbf{F}_{\frac{2}{3}} + \mathbf{F}_1$

Table 5.2: Osher-Solomon flux formulae for the Euler equations using O-ordering of the integration paths, $\mathbf{F}_k = \mathbf{F}(\mathbf{U}_k)$ [20]

6 The 2nd Order Approach

To get more accurate, smooth results, for the Riemann problem, it is desirable to take the approximate solvers to higher order. In order to take the approximate Riemann solvers to higher order, we need to look at various schemes that enable us to do so. Some various examples are given by Toro [20], and for this study we will use the centred total variation diminishing (TVD) scheme.

Godunov's theorem proves that only first order linear schemes preserve monotonicity and are therefore TVD. Although higher order linear schemes are more accurate for smooth solutions, they are not TVD and have a tendancy to introduce spurious oscillations, or wiggles, where discontinuities or shocks arise. In order to overcome this drawback, we use flux limiters.

6.1 The FORCE Flux

Recapping the hyperbolic conservation laws

$$\mathbf{U}_t = \mathbf{F}(\mathbf{U})_x = 0 \tag{6.1}$$

such as the Euler equations (from previous chapter state which), which can be solved using a classical scheme of first order accuracy such as that of Lax-Friedrichs. In the Lax scheme, the numerical flux at the interface of two states $\mathbf{U}_L$, $\mathbf{U}_R$ is

$$\mathbf{F}^{LF}_{i+\frac{1}{2}} = \mathbf{F}^{LF}_{i+\frac{1}{2}}(\mathbf{U}_L, \mathbf{U}_R) = \frac{1}{2}\left[\mathbf{F}(\mathbf{U}_L) + \mathbf{F}(\mathbf{U}_R)\right] + \frac{1}{2}\frac{\Delta x}{\Delta t}\left[\mathbf{U}_L - \mathbf{U}_R\right]. \tag{6.2}$$

Of interest to us at this stage is the Richtmyer scheme [10], which is a second-order accurate scheme that computes a numerical flux by first defining an intermediate state

$$\mathbf{U}^{RI}_{i+\frac{1}{2}} \equiv \mathbf{U}^{RI}_{i+\frac{1}{2}}(\mathbf{U}_L, \mathbf{U}_R) = \frac{1}{2}(\mathbf{U}_L + \mathbf{U}_R)\frac{\Delta t}{\Delta x}\left[\mathbf{F}(\mathbf{U}_L) - \mathbf{F}(\mathbf{U}_R)\right] \tag{6.3}$$

and then setting

$$\mathbf{F}^{RI}_{i+\frac{1}{2}} = \mathbf{F}(\mathbf{U}^{RI}_{i+\frac{1}{2}}). \tag{6.4}$$

The First Order Centered (FORCE) scheme [18] for non-linear systems had numerical flux

$$\mathbf{F}^{force}_{i+\frac{1}{2}} = \mathbf{F}^{force}_{i+\frac{1}{2}}(\mathbf{U}_L, \mathbf{U}_R) = \frac{1}{2}\left[\mathbf{F}^{LF}_{i+\frac{1}{2}}(\mathbf{U}_L, \mathbf{U}_R) + \mathbf{F}^{RI}_{i+\frac{1}{2}}(\mathbf{U}_L, \mathbf{U}_R)\right]. \tag{6.5}$$

6.2 Flux Limiter Centered Scheme

The general approach for the flux limiter scheme combines a low order monotone flux $\mathbf{F}^{LO}_{i+\frac{1}{2}}$ and a high order $\mathbf{F}^{HI}_{i+\frac{1}{2}}$ as

$$\mathbf{F}_{i+\frac{1}{2}} = \mathbf{F}^{LO}_{i+\frac{1}{2}} + \phi_{i+\frac{1}{2}}\left[\mathbf{F}^{HI}_{i+\frac{1}{2}} - \mathbf{F}^{LO}_{i+\frac{1}{2}}\right], \tag{6.6}$$

where $\phi_{i+\frac{1}{2}}$ is a flux limiter. We can construct a Flux LImiter Centered (FLIC) scheme by taking

$$\mathbf{F}^{LO}_{i+\frac{1}{2}} \equiv \mathbf{F}^{force}_{i+\frac{1}{2}};\ \mathbf{F}^{HI}_{i+\frac{1}{2}} \equiv \mathbf{F}^{RI}_{i+\frac{1}{2}} \tag{6.7}$$

where $\mathbf{F}^{force}_{i+\frac{1}{2}}$ and $\mathbf{F}^{RI}_{i+\frac{1}{2}}$ are the fluxes for FORCE and Richtmyer schemes given by (6.5) and (6.4). For analysis of the scalar version of this scheme, refer to Toro [20], but for this we need only consider that the analysis contains wave propagation information via the Courant number c. A relationship between conventional upwind flux limiters $\psi(r)$ and centred flux limiters $\phi(r)$ is as follows (see [**?**] Sect. 13.7.4 for derivation)

$$\phi(r) = \hat{\phi}_g + (1 - \hat{\phi}_g)\psi(r), \tag{6.8}$$

with

$$\hat{\phi}_g = \begin{cases} 0,\ r \leqslant 1, \\ \phi_g \equiv (1 - c_{max})/(1 + c_{max}),\ r \geqslant 1. \end{cases} \tag{6.9}$$

By setting, for example, $c_{max} = C_{cfl}$, the function ϕ_g retains some upwinding at no extra cost. We now choose the following symmetric upwind flux limiters to obtain centred flux limiters, minmod [13], superbee [13] and van Leer [21]

Minmod

$$\phi_{sb}(r) = \begin{cases} 0, \ r \leqslant 0, \\ 2r, \ 0 \leqslant \mathrm{r} \leqslant \frac{1}{2}, \\ 1, \ \frac{1}{2} \leqslant r \leqslant 1, \\ \min\left\{2, \phi_g + (1-\phi_g)r\right\}, \ r > 1. \end{cases} \tag{6.10}$$

Superbee

$$\phi_{vl}(r) = \begin{cases} 0, \ r \leqslant 0, \\ \frac{2r}{1+r}, \ 0 \leqslant \mathrm{r} \leqslant 1, \\ \phi_g + \frac{2(1-\phi_g)r}{1+r}, \ r \geqslant 1. \end{cases} \tag{6.11}$$

van Leer

$$\phi_{vl}(r) = \begin{cases} 0, \ r \leqslant 0, \\ r, \ 0 \leqslant \mathrm{r} \leqslant 1, \\ 1, \ r \geqslant 1. \end{cases} \tag{6.12}$$

Defining the total energy $q \equiv E$ and setting

$$r^L_{i+\frac{1}{2}} = \frac{\Delta q_{i-\frac{1}{2}}}{\Delta q_{i+\frac{1}{2}}}; \ r^R_{i+\frac{1}{2}} = \frac{\Delta q_{i+\frac{3}{2}}}{\Delta q_{i+\frac{1}{2}}}. \tag{6.13}$$

And then we compute a single flux limiter

$$\phi^{LR} = \min\left\{\phi(r^L_{i+\frac{1}{2}}), \phi(r^R_{i+\frac{1}{2}})\right\}, \tag{6.14}$$

where ϕ is any of the limiter functions (6.10)-(6.13). The single limiter $\phi^(LR$ is then applied to all three flux components in (6.6). A general approach for a system whose vector of conserved variables has components $u_k, k = 1, ..., m$ is to apply (6.13)-(6.14) to every component u_k and obtain a limiter of ϕ_k^{LR}. Then we can select the final limiter as

$$\phi^{LR} = \min_k(\phi_k^{LR}), \ k = 1, ..., m \ .$$

7 Comparison of Schemes

All schemes required tweaking of CFL for each test case. In all tests, data consists of two constant states $\mathbf{W}_L = [\rho_L, u_L, p_L]^T$ and $\mathbf{W}_R = [\rho_R, u_R, p_R]^T$ with a discontinuity in the middle of the states at position $x = x_0$. Numerical solutions are presented with exact solutions and are found in the domain $0 \leq x \leq 1$. The exact solver was provided by Dr Sweby [16] and was coded from Smoller's equations.

7.1 Roe

To test the Roe scheme we used slight variations of the problems described in Section 2.3. These are presented in Table 7.1. All tests were performed as ideal gases with $\gamma = 1.4$ and compared to the exact solution. All chosen data consists of two constant states separated by a discontinuity at $x = x_0$, the position of which is chosen for convenience with each test and is stated in the legend. The exact and numerical solutions are found in the spatial domain $0 \leq x \leq 1$ and the numerical solution is computed with $M = 100$ cells and a CFL of 0.5.

Test	ρ_L	u_L	p_L	ρ_R	u_R	p_R
1	1.0	0.75	1.0	0.125	0.0	0.1
2	1.0	-2.0	0.4	1.0	2.0	0.4
3	1.0	0.0	1000.0	1.0	0.0	0.01
4	5.99924	19.5975	460.894	5.99242	-6.19633	46.0950
5	1.0	-19.59745	1000.0	1.0	-19.59745	0.01

Table 7.1: Data for five Riemann problem tests with exact solution for testing the Roe Riemann solver

We modify Sod's problem (2.8) for Test 1, where the solution has a right shock wave, a right travelling contact wave and a left sonic rarefaction wave. We use this test to assess the entropy satifaction property of Roe's solver. The results for this test are shown in Figure 7.1 against the exact results and we can see that the accuracy of the numerical results is nearly indistinguishable from those of the exact Riemann solver, and are particularly accurate around the sonic point.

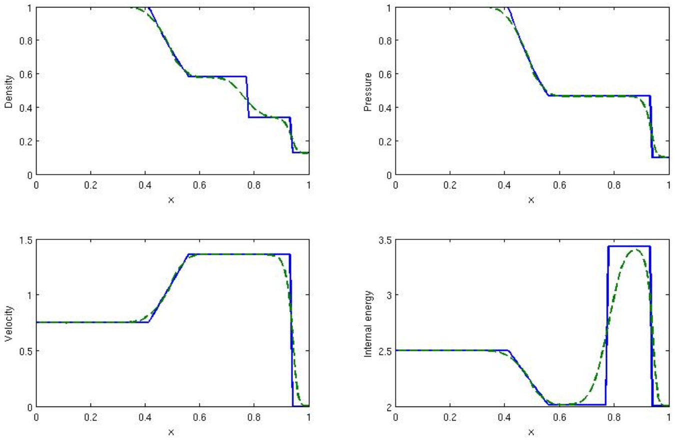

Figure 7.1: Roe Riemann solver applied to Test 1 of Table 7.1. Numerical (dash) and exact (line) solutions compared at time 0.2

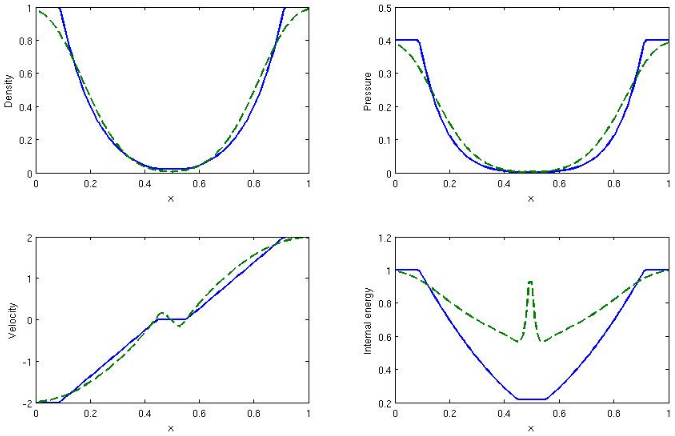

Figure 7.2: Roe Riemann solver applied to test 2 of Table 7.1. Numerical (dash) and exact (line) solutions compared at time 0.15

Test 2 consists of two symmetric rarefaction waves and a trivial contact wave, with the star region between the non-linear waves close to vacuum. This problem is a good assessment of the performance of numerical methods for low-density flows. Reviewing the results in Figure 7.28, we can see that the Roe solver fails near low-density flows. The test contains strong rarefactions with low density and pressure regions in the middle and the solver does fail here.

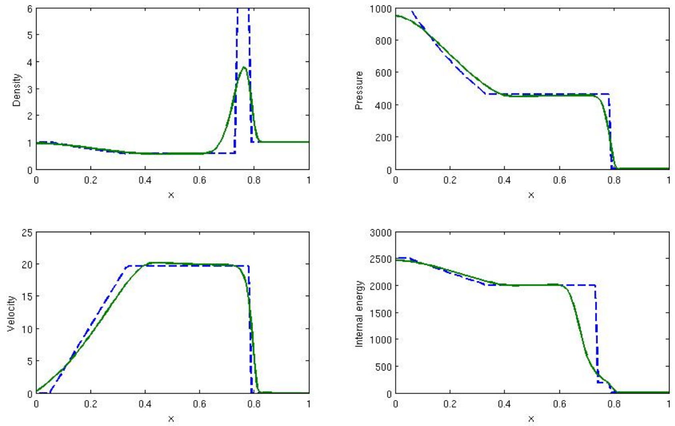

Figure 7.3: Roe Riemann solver applied to test 3 of Table 7.1. Numerical (dash) and exact (line) solutions compared at time 0.012

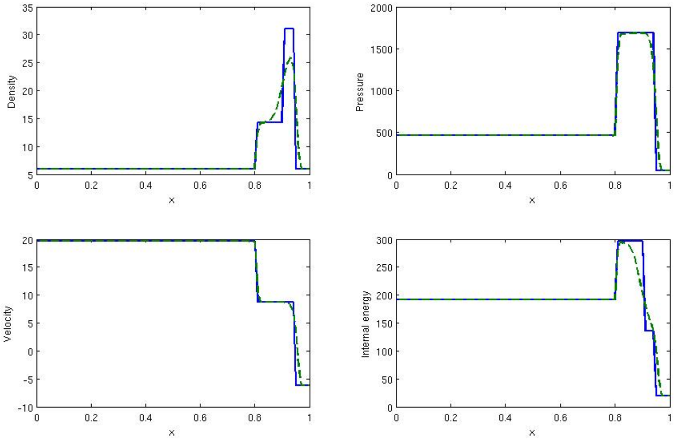

Figure 7.4: Roe Riemann solver applied to test 4 of Table 7.1. Numerical (dash) and exact (line) solutions compared at time 0.012

The robustness and accuracy of the Roe solver is tested with Test 3. The solution of Test 3 consists of a strong shock wave with Mach number 198, a contact surface and a left rarefaction wave. Test 4 is an additionally severe test, consisting of three strong right-travelling discontinuities. We can see from Figures 7.31 and 7.34 that the Roe solver struggles slightly with the density, but otherwise performs very close to the exact solution, with particularly accurate results in Test 4.

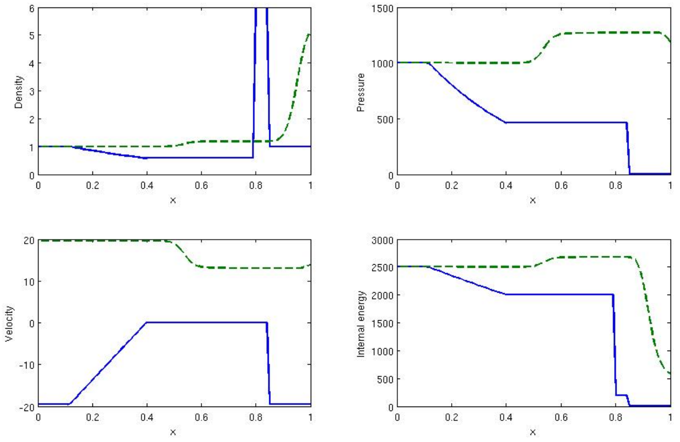

Figure 7.5: Roe Riemann solver applied to test 5 of Table 7.1. Numerical (dash) and exact (line) solutions compared at time 0.012

The final test for the Roe solver is designed to test the robustness of the scheme, but additionally to assess the ability to resolve slow-moving contact discontinuities. The exact solution of Test 5 is made up of a left rarefaction wave, a right-travelling shock wave and a stationary contact discontinuity. From Figure 7.5 we can see that the scheme devised produces extremely inaccurate results and therefore is shown not the be capable of handling this type of discontinuity. This may be resolved using modifications of the Roe solver.

7.2 HLL and HLLC

When investigating the HLL solver, it was neccessary to first make a choice of wave speed estimate. In order to do that the estimates discussed in Section 5.2.2 were investigated, these results are presented first. Following this are slightly modified versions of the Riemann problems introduced in Section 2.3, a table is given of these problems.

7.2.1 Wave speed estimates

The various wave speeds presented in Section 5.2.2 were tested on the Sod's Shock Tube problem (2.8), with $x_0 = 0.5$, to see which would provide the most accurate result for the least expensive computation. Throughout the tests the CFL was kept at 0.5. It was found that the wave speed calculation given by (5.47) was not capable of producing results at higher iterations like the other wave speed estimates were, therefore it was discarded and the results are not shown here. If we consider Figures 7.6 to 7.11 we can see that there is little deviation in precision, but considering the Figures 7.8 and 7.9 we can see that the Roe eigenvalue estimates (5.49) provide disappointing results, as do the Davis estimates (5.53) and these were also not considered. The simpler estimates (5.47) and (5.48), shown in Figures 7.6 and 7.7 respectively, gave fairly accurate results for their computational simplicity, but ultimately Einfeldt's estimate (5.55) shown in Figure 7.10 was more accurate, and simple enough, so this was chosen as the wave speed estimate for all following tests using the HLL scheme. The final wave speed estimate, the PVRS estimate, was shown in Figure 7.11 to be as precise as Einfeldt, thus sufficient for the HLLC scheme that requires the pressure value for the star region.

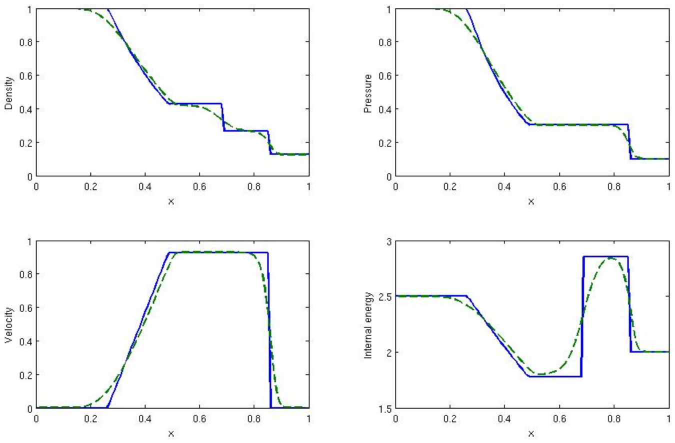

Figure 7.6: HLL Riemann solver applied to Sod's shock tube, using wave speed estimate (5.48). Numerical (dash) and exact (line) solutions compared at time 0.20

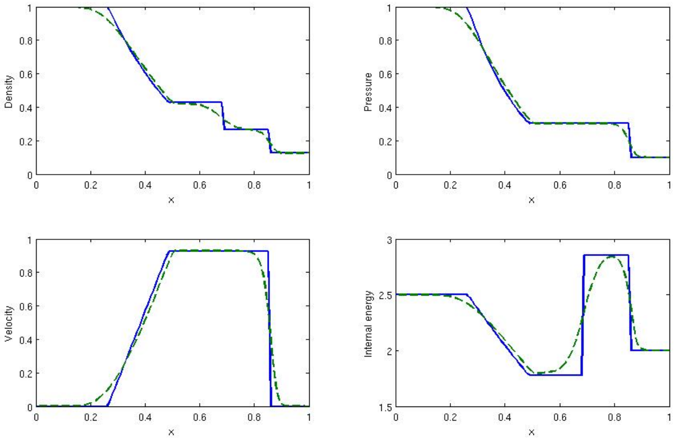

Figure 7.7: HLL Riemann solver applied to Sod's shock tube, using wave speed estimate (5.49). Numerical (dash) and exact (line) solutions compared at time 0.20

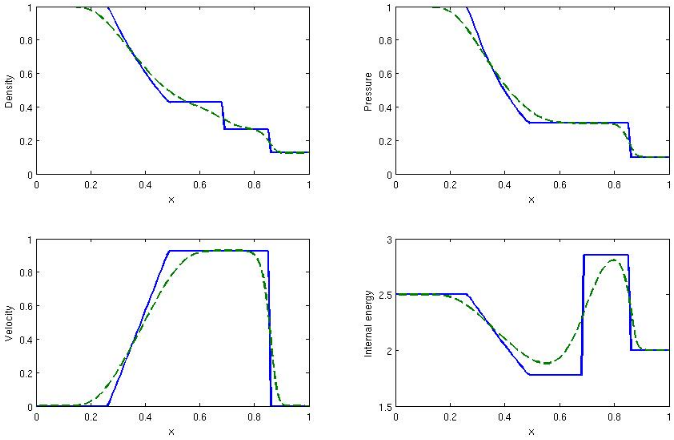

Figure 7.8: HLL Riemann solver applied to Sod's shock tube, using wave speed estimate (5.53). Numerical (dash) and exact (line) solutions compared at time 0.20

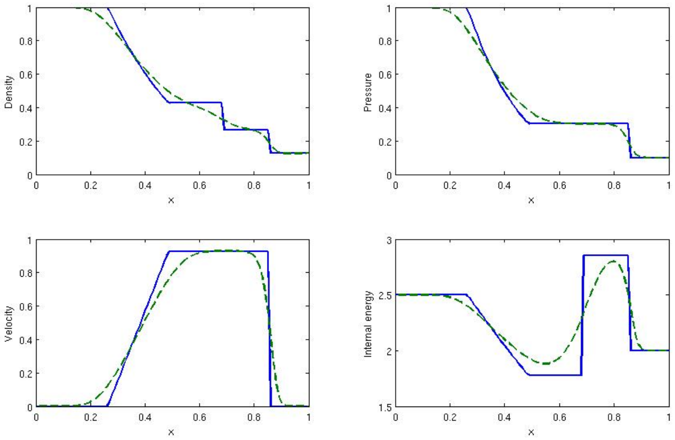

Figure 7.9: HLL Riemann solver applied to Sod's shock tube, using wave speed estimate (5.54). Numerical (dash) and exact (line) solutions compared at time 0.20

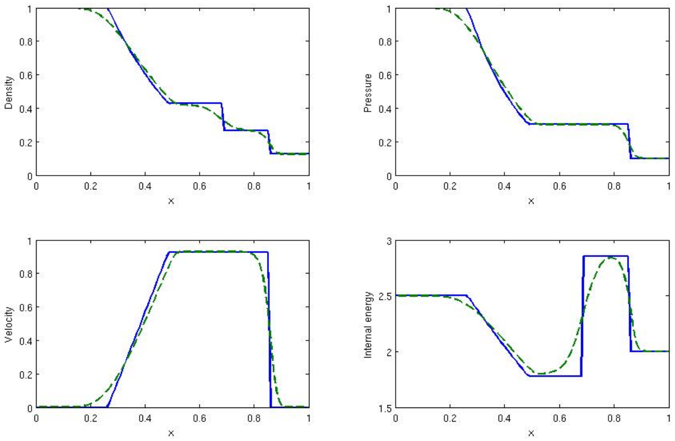

Figure 7.10: HLL Riemann solver applied to Sod's shock tube, using wave speed estimate (5.55). Numerical (dash) and exact (line) solutions compared at time 0.20

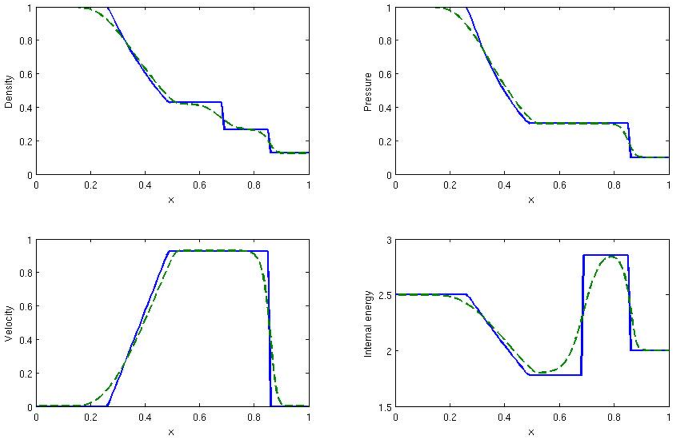

Figure 7.11: HLL Riemann solver applied to Sod's shock tube, using wave speed estimate (5.58). Numerical (dash) and exact (line) solutions compared at time 0.20

7.2.2 Test problems

To test the HLL scheme, modified versions of the problems described in Section 2.3, outlined in Table 7.2. Numerical solutions are computed with $M = 100$ cells. Boundary conditions are transparent with the exception of the blast wave tests, which use reflective boundaries, due to walls being present at either side of the domain.

Test	ρ_L	u_L	p_L	ρ_R	u_R	p_R
1	1.0	0.75	1.0	0.125	0.0	0.1
2	1.0	-2.0	0.4	1.0	2.0	0.4
3	1.0	0.0	1000.0	1.0	0.0	0.01
4	5.99924	19.5975	460.894	5.99242	-6.19633	46.0950
5	1.0	-19.5975	1000.0	1.0	-19.5975	0.01
6	1.4	0.0	1.0	1.0	0.0	1.0
7	1.4	0.1	1.0	1.0	0.1	1.0

Table 7.2: Data for test problems for the HLL and HLLC schemes

These tests were first presented by Toro [20] in order to assess specific parts of the schemes. All were conducted as ideal gases with $\gamma = 1.4$, with two constant states separated by a discontinuity at $x = x_0$. The exact and numerical solutions are found in the domain $0 \leq x \leq 1$, and the numerical solutions were computed with $M = 100$ cells and the CFL was kept at 0.5. Boundary conditions are transparent with the exception of tests based on the blast wave problem. For each problem a convenient location for x_0 is chosen and stated in the legend.

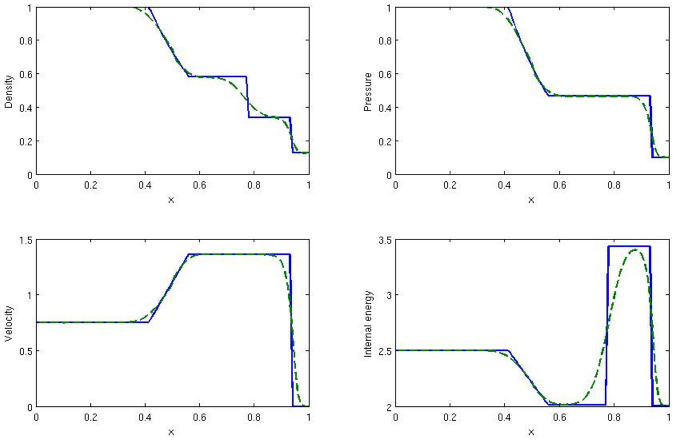

Figure 7.12: HLL Riemann solver applied to Test 1 of Table 7.2. Numerical (dash) and exact (line) solutions compared at time 0.2 and $x_0 = 0.5$

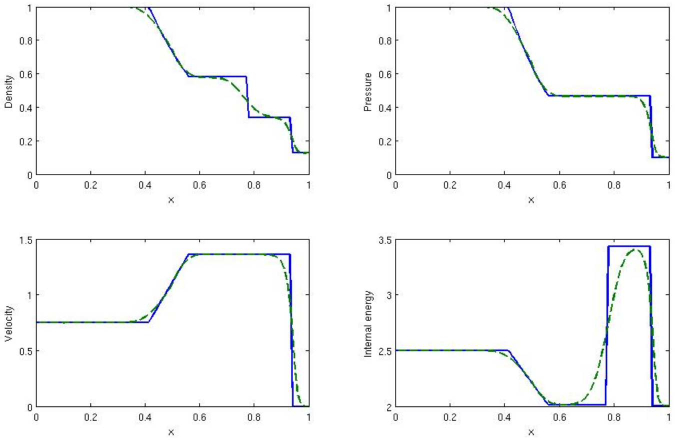

Figure 7.13: HLLC Riemann solver applied to Test 1 of Table 7.2. Numerical (dash) and exact (line) solutions compared at time 0.2 and $x_0 = 0.5$

For test 1, the Sod's Shock Tube problem (2.8) was modified slightly. The solution of the problem has a right shock wave, a right travelling contact wave and a left sonic rarefaction wave. The purpose of this test is to assess the entropy satisfaction property of the numerical methods. Figures 7.12 and 7.13 show the exact results against the HLL and HLLC schemes respectively. An important point to note here is that the sonic rarefaction, the reduction of the density, is better resolved by the HLL and HLLC solvers than by the exact solution. Its also worth noting that neither HLL or HLLC is clearly superior in its handling to the other.

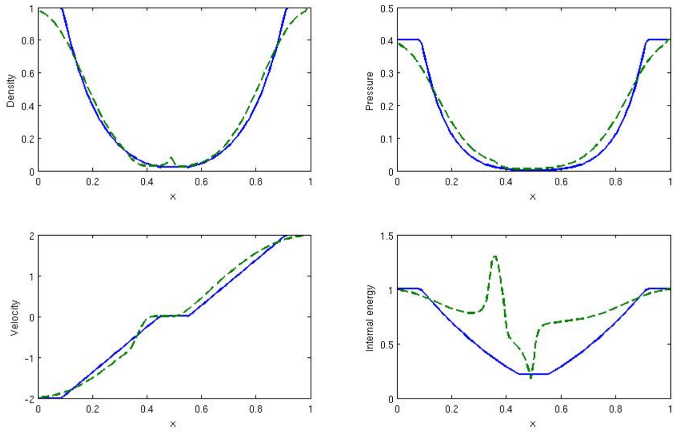

Figure 7.14: HLLC Riemann solver applied to Test 2 of Table 7.2. Numerical (dash) and exact (line) solutions compared at time 0.15 and $x_0 = 0.5$

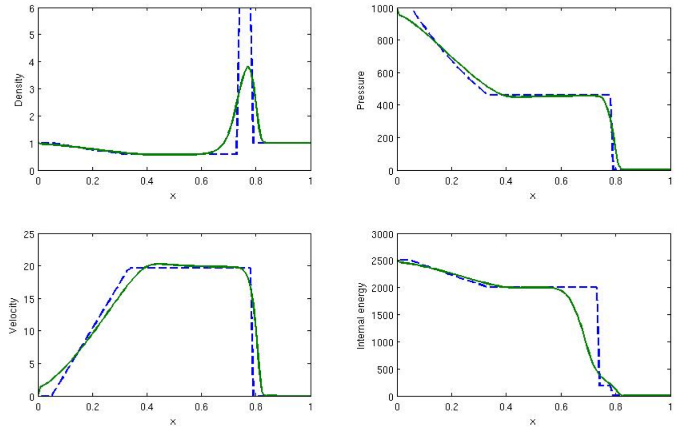

Figure 7.15: HLL Riemann solver applied to the left-hand side of the Blast Wave problem, Test 3 of 7.2. Numerical (dash) and exact (line) solutions compared at time 0.012 and $x_0 = 0.5$

Test 2's solution concerns itself with two symmetric rarefaction waves and a trivial contact wave. Between the linear waves, the star region is close to vacuum, making the problem a good test for assessing the performance of the approximate Riemann solvers for low-density flows. The first point to note is that the HLL solver was not robust enough to produce satisfactory results for this test, and has therefore not been plotted. The HLLC solver, shown in Figure 7.27, produced fairly accurate results, but broke down when dealing with the internal energy of the system.

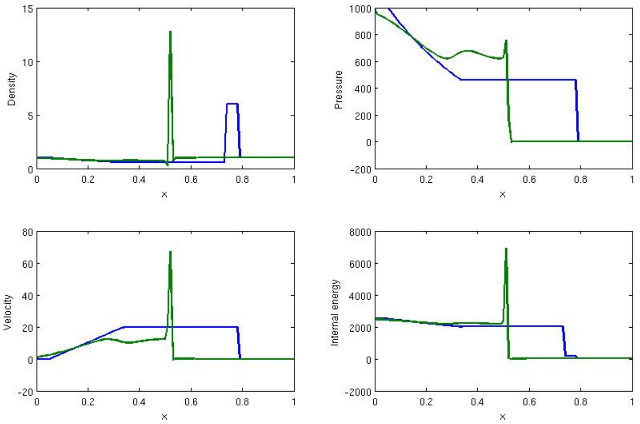

Figure 7.16: HLLC Riemann solver applied to Test 3 of Table 7.2. Numerical (dash) and exact (line) solutions compared at time 0.012 and $x_0 = 0.5$

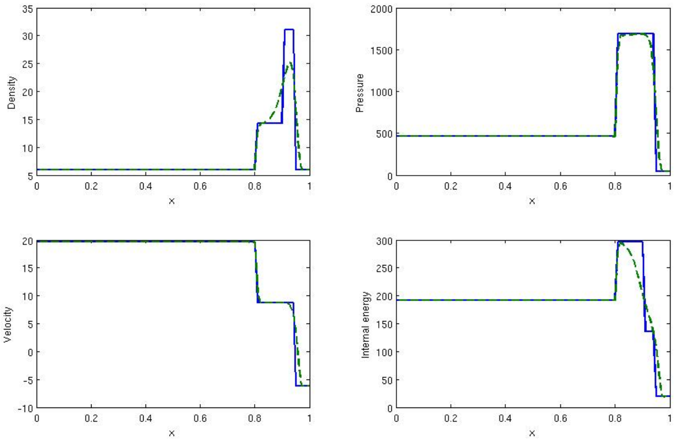

Figure 7.17: HLL Riemann solver applied to Test 4 of Table 7.2. Numerical (dash) and exact (line) solutions compared at time 0.012 and $x_0 = 0.4$

Accuracy and robustness is tested using test 3, the solution of which consists of a strong shock wave, a contact surface and a left rarefaction wave. The strong shock wave is of Mach number 198, where the Mach number is the speed of an object moving through a fluid divided by the speed of sound in that fluid for its particular physical conditions, including those of temperature and pressure, it is a dimensionless quantity. We can see in Figure 7.29 that the HLL scheme is fairly robust, but struggles somewhat to represent accurate density, this result is unexpected as we would expect it to perform better than the HLL solver.

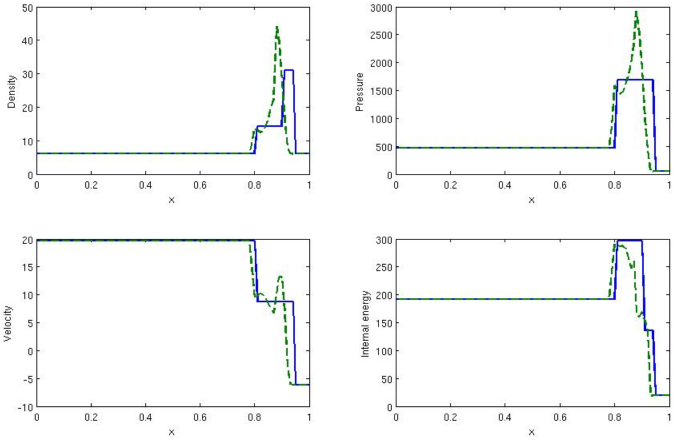

Figure 7.18: HLLC Riemann solver applied to Test 4 of Table 7.2. Numerical (dash) and exact (line) solutions compared at time 0.012 and $x_0 = 0.4$

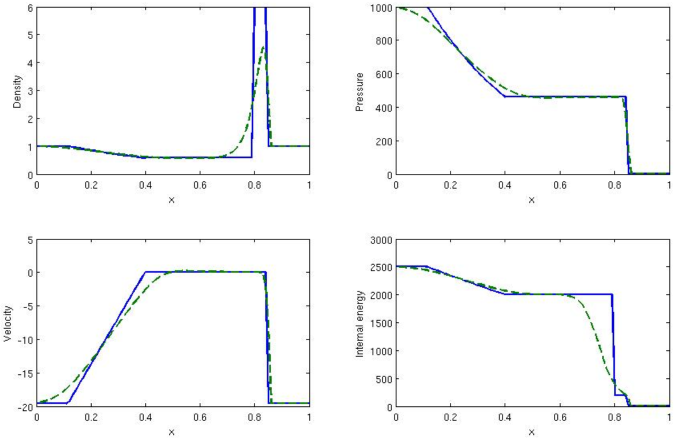

Figure 7.19: HLL Riemann solver applied to Test 5 of 7.2. Numerical (dash) and exact (line) solutions compared at time 0.012 and $x_0 = 0.8$

Another severe test is used in test 4. This time the solution consists of three strong discontinuities travelling to the right. Again HLL out-performs HLLC, which is unexpected.

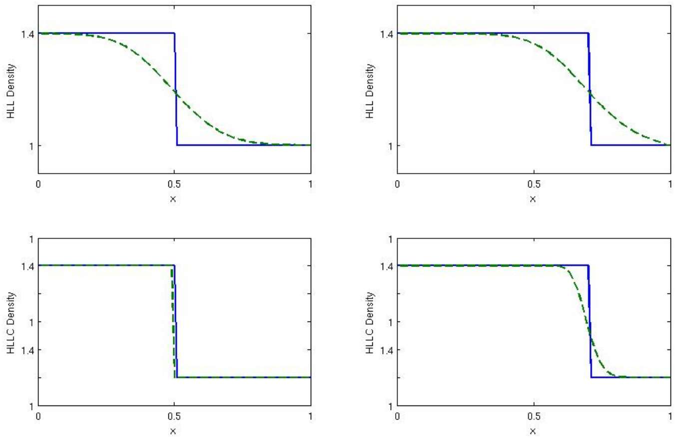

Figure 7.20: Density profiles for the HLL and HLLC Riemann solvers applied to tests 6 and 7, with wave speed estimate Einfeldt (5.55). Numerical (dash) and exact (line) solutions compared at time 0.20

The solution of test 5 consists of a right-travelling shock wave, a left rarefaction wave and a stationary contact discontinuity. Looking at Figure 7.19, we can see that the HLL Riemann solver diffuses the contact wave to less precise levels. This should highlight the advantage of HLLC over HLL in the resolution of slowly-moving contact discontinuities, however we were unable to produce a satisfactory result with the HLLC scheme. This observation is however emphasised by Tests 6 and 7. Tests 6 and 7 shown in Figure 7.20 show the likely performance of the HLL and HLLC solvers for contacts, shear waves and vortices. Specifically the figure shows the results for an isolated contact wave, where the HLLC preserves the entropy satisfaction property of the HLL solver. The HLL solver shows itself to give smeared results for stationary and slowly moving contact waves, whereas the HLLC behaves exactly as the exact Riemann solver for this problem. The HLLC scheme gives infinite resolution for stationary contact waves and the numerical dissipation for slowly moving contacts is much less.

7.3 Osher

The Osher-Solomon scheme proved to be very elaborate to code. Despite numerous attempts to produce a working scheme in FORTRAN-95, we could not escape wild fluctuations at the discontinuities. The scheme, like others, was aimed to be subject to several tests, presented in Table 7.3.

Test	ρ_L	u_L	p_L	ρ_R	u_R	p_R
1	1.0	0.75	1.0	0.125	0.0	0.1
2	1.0	-2.0	0.4	1.0	2.0	0.4
3	1.0	0.0	1000.0	1.0	0.0	0.01
4	5.99924	19.5975	460.894	5.99242	-6.19633	46.0950
5	1.0	-19.59745	1000.0	1.0	-19.59745	0.01
6	1.0	2.0	0.1	1.0	-2.0	0.1

Table 7.3: Data for five Riemann problem tests

Figures 7.21 to 7.22 show the Osher-Solomon scheme with P-ordering on several basic numerical tests. The fact that the scheme failed to even produce results for 7.21 shows that there is an error in the code, as opposed to an error in the scheme. We would expect to see results for all six tests with P-ordering, with Tests 1 to 4 being equally accurate to the exact solver, but with severe oscillations around the shocks in Test 6. We would expect O-ordering to fail on both Tests 2 and 6. And for Test 5 we would expect P-ordering to produce an incorrect solution. Toro notes that Test 5 produces very large unphysical overshoots in density, velocity and pressure and that the right-travelling shock fails to propagate at all. Toro goes on to note that the shock wave appears not to form and that incorrect values are produced behind the contact discontinuity. Unfortunately, the code used was unable to recreate these tests accurately with the exception of the simple Shock Tube, shown in Figure 7.21.

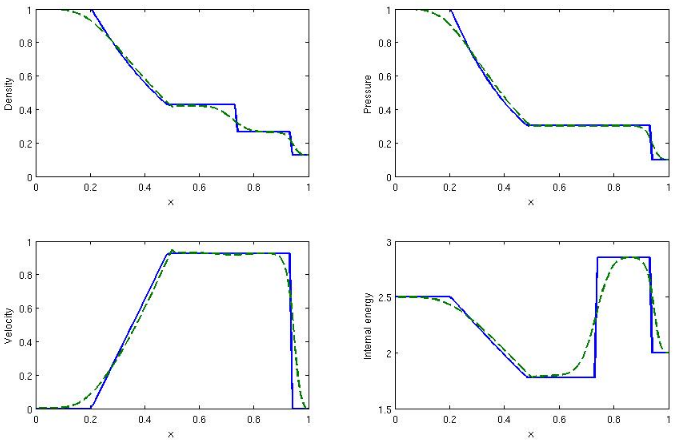

Figure 7.21: Osher Riemann solver applied to Test 1 of Table 7.3, with P-ordering. Numerical (dash) and exact (line) solutions compared at time 0.2

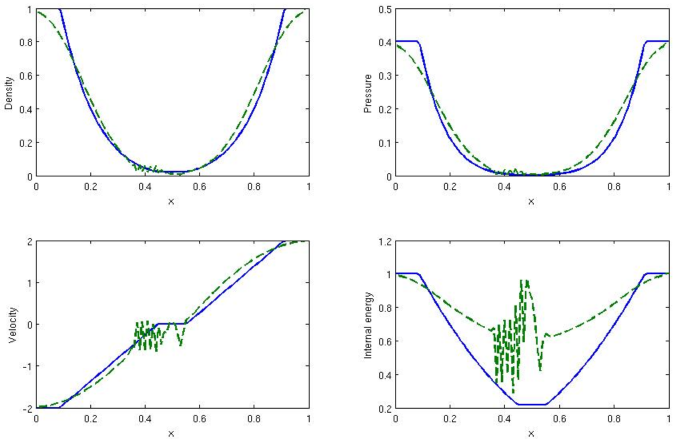

Figure 7.22: Osher-Solomon Riemann solver applied to test 2 of Table 7.3, with P-ordering. Numerical (dash) and exact (line) solutions compared at time 0.15

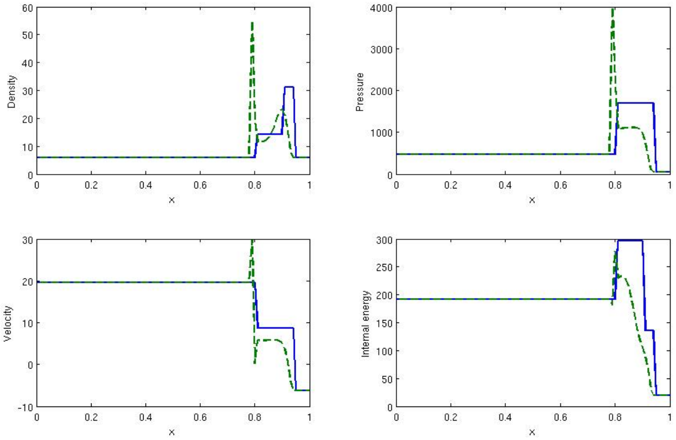

Figure 7.23: Osher-Solomon Riemann solver applied to test 4 of Table 7.3, with P-ordering. Numerical (dash) and exact (line) solutions compared at time 0.012

7.4 The tests

Here we use the tests originally presented in Section 2.3. We recap on these tests in Table 7.4

Test	ρ_L	u_L	p_L	ρ_R	u_R	p_R
1	1.0	0.0	1.0	0.125	0.0	0.1
2	1.0	-2.0	0.4	1.0	2.0	0.4
3	1.0	0.0	1000.0	1.0	0.0	0.01
4	1.0	0.0	0.01	1.0	0.0	100.0
5	5.99924	19.5975	460.894	5.99242	-6.19633	46.0950

Table 7.4: Data for five Riemann problem tests

While we used modified versions of these for each solver, we now use the unmodified versions on all schemes, with the exception of the Osher-Solomon scheme, for comparison.

7.4.1 Test 1

Test 1 is the mildest test, and is known as the Sod test problem.It consists of a left rarefaction, a contact and a right shock. Profiles were taken at time $t = 0.25$ and initial position $x_0 = 0.5$. All schemes are adept at handling this problem.

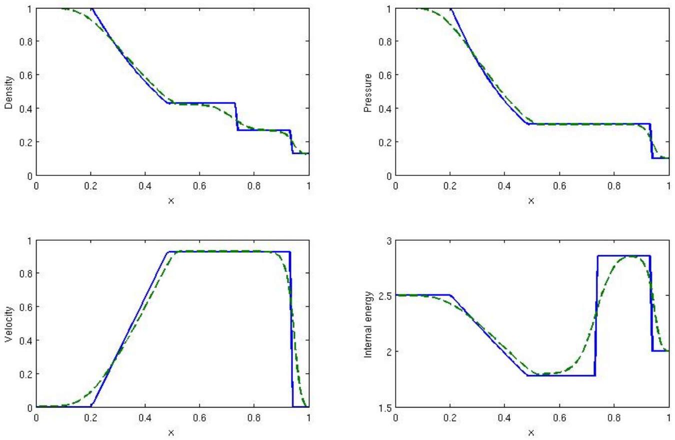

Figure 7.24: HLL Riemann solver applied to test 1 of Table 7.4, with Einfeldt wave speed. Numerical (dash) and exact (line) solutions compared at time 0.25

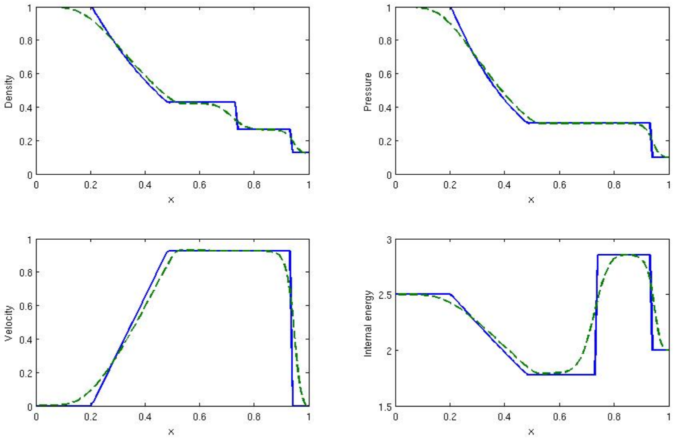

Figure 7.25: HLLC Riemann solver applied to test 1 of Table 7.4. Numerical (dash) and exact (line) solutions compared at time 0.25

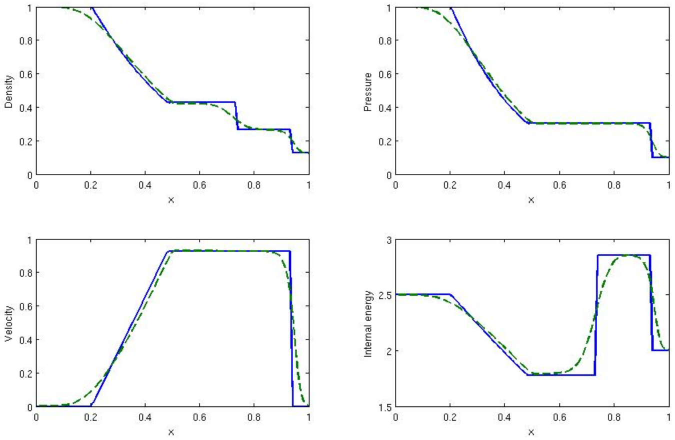

Figure 7.26: Roe Riemann solver applied to test 1 of Table 7.4. Numerical (dash) and exact (line) solutions compared at time 0.25

7.4.2 Test 2

Test 2 is otherwise known as the *123 problem*. Consisting of two strong rarefactions and a trivial stationary contact discontinuity. Profiles were taken at time $t = 0.15$ and initial position $x_0 = 0.5$. The HLL scheme did not produce sufficient results to enable plotting of a graph, with the scheme breaking down early. One of the most notable points is that none of the schemes very sufficiently give accurate results for the specific internal energy.

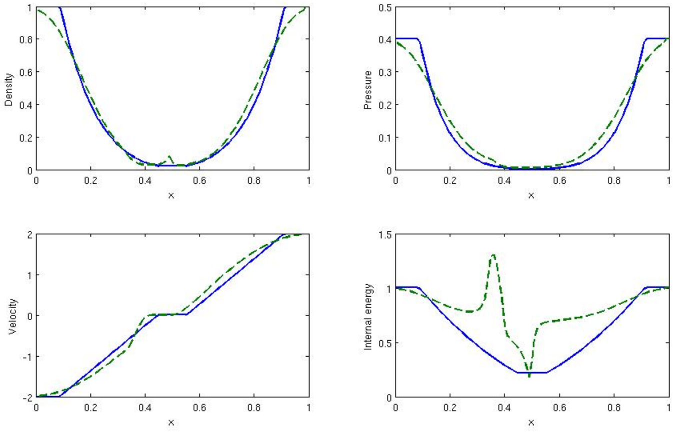

Figure 7.27: HLLC Riemann solver applied to test 2 of Table 7.4. Numerical (dash) and exact (line) solutions compared at time 0.15

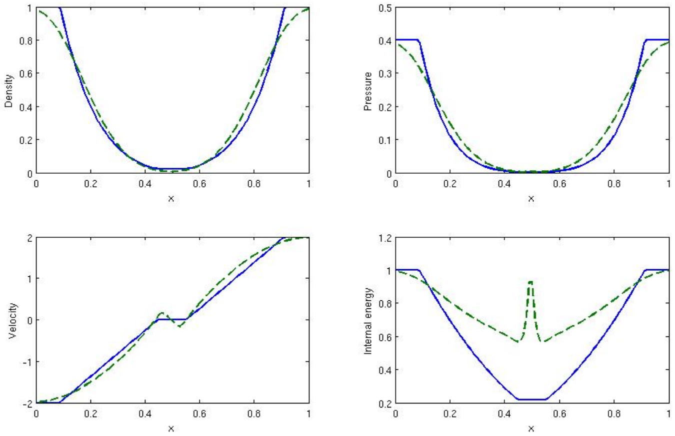

Figure 7.28: Roe Riemann solver applied to test 2 of Table 7.4. Numerical (dash) and exact (line) solutions compared at time 0.15

7.4.3 Test 3

Test 3 represents the left-hand side of the blast wave problem.

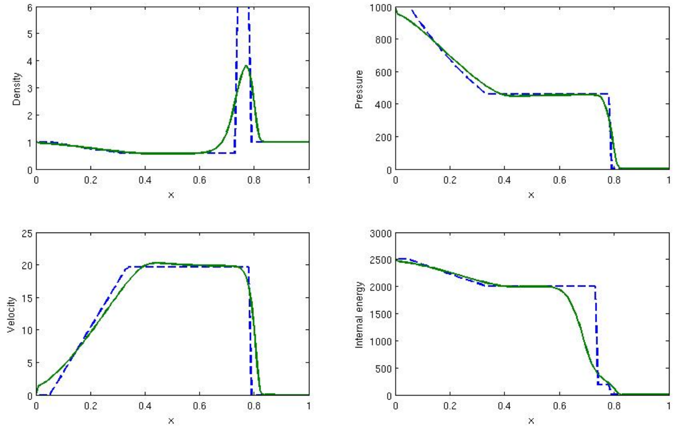

Figure 7.29: HLL Riemann solver applied to test 3 of Table 7.4. Numerical (dash) and exact (line) solutions compared at time 0.012

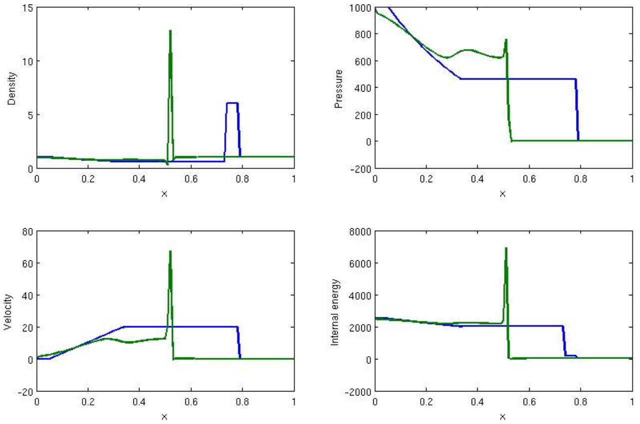

Figure 7.30: HLLC Riemann solver applied to test 3 of Table 7.4. Numerical (dash) and exact (line) solutions compared at time 0.012

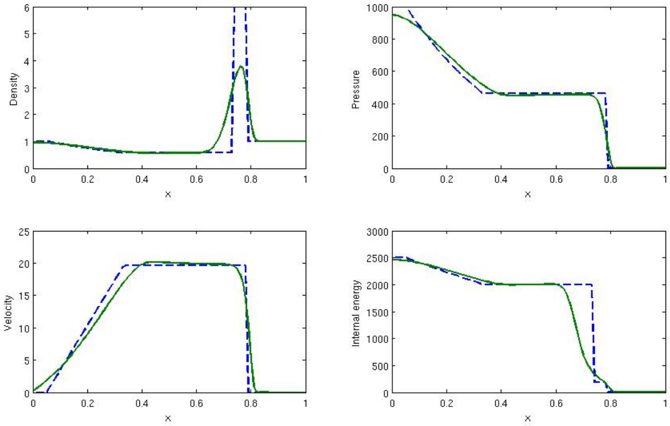

Figure 7.31: Roe Riemann solver applied to test 3 of Table 7.4, with P-ordering. Numerical (dash) and exact (line) solutions compared at time 0.012

7.4.4 Test 5

Recall that test 5 is made up from right and left shocks emerging from the solution of the blast wave problem of tests 3 and 4. The solution of test 5 represents the collision of two strong shocks and consists of a left facing shock travelling slowly right, a right travelling contact discontinuity and a right travelling shock wave [20]. Profiles were taken at time $t = 0.012$ and initial position $x_0 = 0.8$.

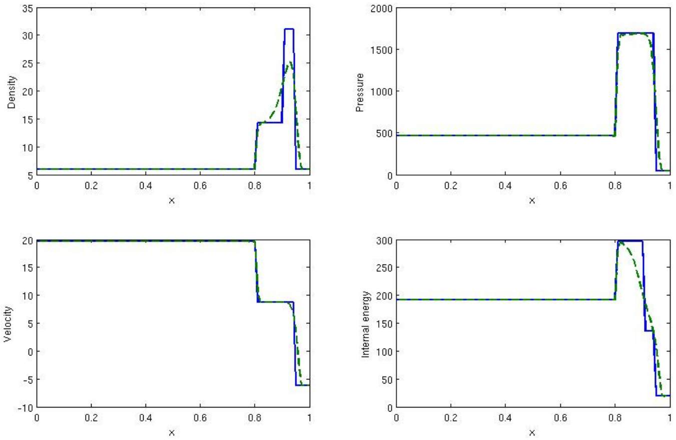

Figure 7.32: HLL Riemann solver applied to test 5 of Table 7.4, with Einfeldt wave speed. Numerical (dash) and exact (line) solutions compared at time 0.012

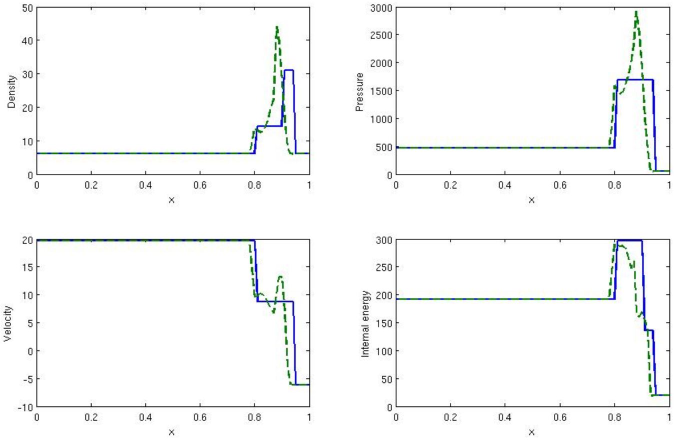

Figure 7.33: HLLC Riemann solver applied to test 5 of Table 7.4. Numerical (dash) and exact (line) solutions compared at time 0.012

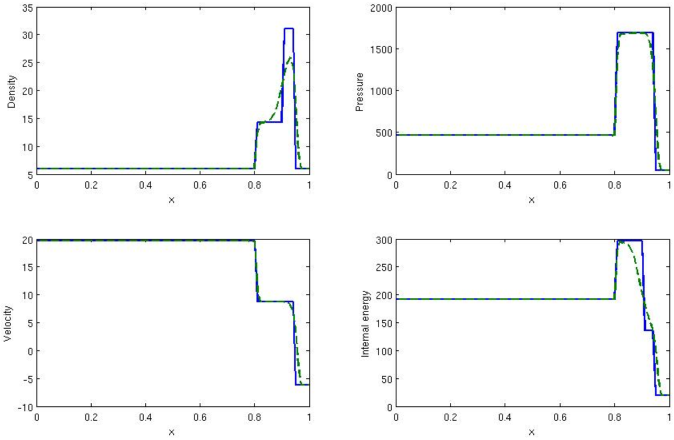

Figure 7.34: Roe Riemann solver applied to test 5 of Table 7.4. Numerical (dash) and exact (line) solutions compared at time 0.012

7.5 Second Order Results

It is desirable to produce higher order results for the schemes as this significantly improves the accuracy. In this section the results of the method described in Section 6 as applied to the Riemann solver of Roe are presented. Each test was performed using Sod's shock tube (2.8), with the discontinuity at $x_0 = 0.5$ to demonstrate how much more accurate the scheme is at second order. For all tests the one-dimensional time dependent Euler equations were used as ideal agses with $\gamma = 1.4$. The exact and numerical solutions are found in the spatial domain $0 \leq x \leq 1$. The numerical solutions are computed with $M = 100$ and the CFL is 0.5.

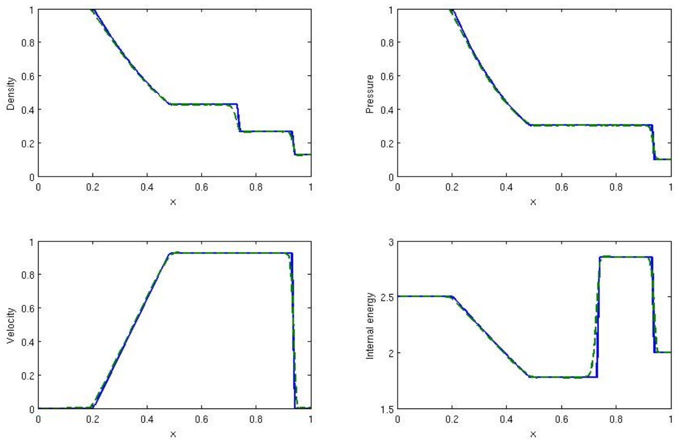

Figure 7.35: Flux Limiter Scheme for second order with Roe Riemann solver and Superbee applied to Sod's shock tube problem (refeq:sod). Numerical (dash) and exact (line) solutions at time t= 0.25

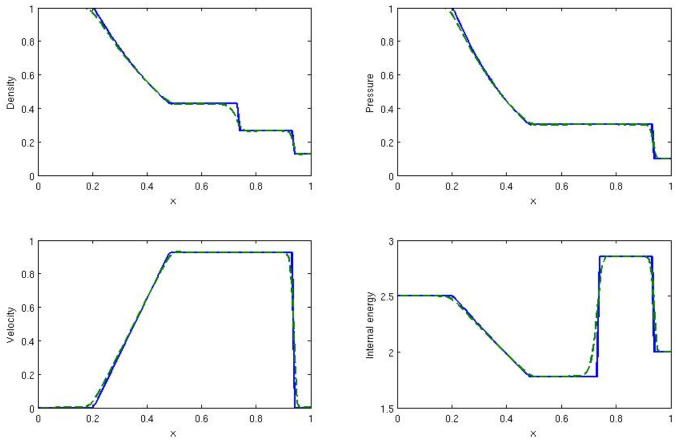

Figure 7.36: Flux Limiter Scheme for second order with Roe Riemann solver and van Leer applied to Sod's shock tube problem (refeq:sod). Numerical (dash) and exact (line) solutions at time t= 0.25

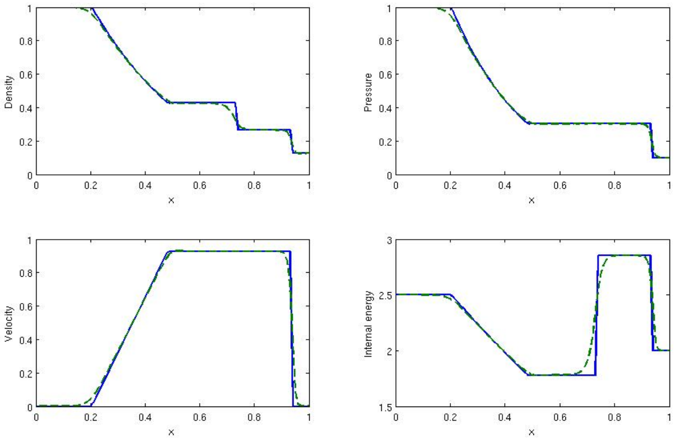

Figure 7.37: Flux Limiter Scheme for second order with Roe Riemann solver and Minmod applied to Sod's shock tube problem (refeq:sod). Numerical (dash) and exact (line) solutions at time t= 0.25

8 Discussion

This section aims to clarify what is shown in the results section and expand on how the study can be further improved. We will look at the results given in Section 7 separately and hollistically to compare and contrast the various Riemann solvers presented. We will also discuss how these tests may be extended and improved upon for future study.

To first consider the Roe Riemann solver and the tests performed in Section 7.1, we have found some notable faults in the scheme. One fault is that Test 2 showed the failure of the scheme near low-density flows. Einfeldt et al. [5] have provided methodology that can be used to modify the Roe solver to prevent this failure. This would be of interest in further exploratons of the Roe solver.

However, the Roe solver does prove to be a very powerful solver, having several desirable qualities. It tightly resolves shocks and contact discontinuities; having a significant high resolution. Since it treats shocks directly, it does not need any artifical viscosity for shocks: it *captures* them. In addition it has a very low numerical diffusivity and is strictly conserving in mass, momentum and energy. Sound waves are propagated with precision, as the scheme treats pressure gradients as characteristics. Overall, it is a stable and non-viscous scheme, proving itself to be high-resolution. This is further emphasised by the second-order results, Figures 7.35 to 7.37, where, particularly with the Superbee scheme, Roe's solver becomes indistinguishable from the exact solution.

Next we review the HLL scheme. We would refer to this as an 'incomplete' Riemann solver, as it does not contain the full set of waves present in the exact solution. This lack of intermediate waves leads to problems, in particular with entropy waves, slip surfaces, material interfaces, vortical flows, ingniton fronts, shear layers, and as demonstrated, contact discontinuities. The HLL scheme showed its weakness giving unacceptably smeared results for stationary and slowly moving contact waves. The HLLC solver, however, in tests 6 and 7 behaved like the exact Riemann solver showing itself to be an improved version of the HLL scheme. The HLLC scheme should have shown good results for Tests 3 to 5, however it did not. It is not clear where the error lied but it is possible the chosen wave speed calculation was not sufficient. Other wave speed estimates for the Star Region are available, and further investigation would be warranted to improve the performance of the HLLC scheme, as it is known to perform better than HLL in these regions [20]. Improvement of this scheme is desirable as it would be preferrable to the HLL scheme for further study at higher order.

One of the most unfortunate parts of this study was the failure to reach a working code for the Osher-Solomon scheme. Perhaps, if nothing else, this demonstrates how impratical the scheme is, as the large tables of comparison to choose flux lead to computational and time expense. In order to evaluate flux any code must work through 16 cases for the one-dimensional Euler case. In fact, it is computationally more expensive than the exact solver used in this study. Additionally it has other features that make it unattractive, as it requires a state-Riemann solver to definte intermediate paths and requires sonic point states. Before any attempt can be made to solve numerically, the matrix integral must be solved analytically. Overall the complexities of the scheme essentially restrict it to the Euler equations for ideal gases and make it virtually impossible to apply to complex hyperbolic systems.

Regardless, there are some attractive features of the Osher-Solomon solver which it would have been desirable to see to compare with the Roe and HLL solvers. No entropy fix is required from it and it is robust for strong shocks, low density flows and good performance for slow-moving shocks [20]. It is a 'complete' solver; the wave model contains all characteristic fields of the exact problem. An extended version of the Osher-Solomon solver has been proposed by Dumbser and Toro [3], relying on simple path and numerical integration, which may prove simpler and less expensive to use, although it is aimed at hyperbolic problems.

We can look at these like a hierarcy, complete Riemann solvers that contain in their structure the full set of waves present in the exact solution of the Riemann problem: exact, Roe, Osher-Solomon, HLLC (for the Euler equations), and incomplete Riemann solvers that do not contain in their structure the full set of waves present in the exact solution of the Riemann problem: HLL.

Overall the solvers presented in this study are restricted to the classical case of piece-wise constant data. The 'ultimate' classical solver, that is one that is non-linear and complete, is unavailable at this time. Classical Riemann solvers give the numerical flux for the first-order Godunov upwind method. High-order Gudonov-type methods can be constructed using classical Riemann solvers (at low order).

A desirable extension to this work would be to take the second-order scheme described in Section 6 and apply it to the HLL and HLLC solvers and compare again with the Roe scheme. One could also consider other methods to take the schemes to higher-order, although the Flux Limiting scheme, particularly with the Superbee limiter, seems to be more than sufficient. The natural step on from this would be to introduce more dimensions to problems, using dimension-splitting models or Finite Volume methods. Multi-dimensional problems such as explosions or implosions could then be tested, leading to some very interesting three-dimensional models with perhaps more pratical implications. Reviews of higher-order and multi-dimensional methods can be found in comprehensive texts such as LeVeque [8] and Toro [20].

9 Conclusion

In this paper, we have presented three high-resolution schemes and applied them to approximate Euler equations. Several test cases were used to test the numerical schemes and highlight their strengths and weaknesses. We highlighted how Roe's scheme performed well, however it failed at low-density flows. Overall it was shown to be a robust scheme, performing to exact standards at second order. We then showed how the simple HLL scheme produced good results, a very desirable scheme due to the simplicity-to-accuracy ratio, however it lacked accuracy at some forms of contact discontinuities. We then showed how the HLLC scheme improved on this, however due to some errors we were unable to demonstrate some of its desirable properties and it suffered more diffusion than Roe's scheme. We then looked at the Osher-Solomon scheme, a very expensive and complex scheme, that we were unable to stabilise.

Each scheme performed better for certain test cases, and overall which is the 'best' scheme was inconclusive. Further study was recommended, and the suggestion that there is still no 'ultimate' solver was made.

10 Bibliography

References

[1] Batten, P., Clarke, N., Lambert, C., and Causon, D. On the choice of wave speeds for the hllc riemann solver. *SIAM J. Sci. and Stat. Comp. 18* (1997), 1553–1570.

[2] Davis, S. Simplified second-order gudonov-type methods. *SIAM J. Sci. Stat. Comput. 9* (1988), 445–473.

[3] Dumbser, M., and Toro, E. A simple extension of the osher riemann solver tonon-conservative hyperbolic systems. *Journal of Scientific Computing* (2010), 1–19.

[4] Einfeldt, B. On gudonov-type methods for gas dynamics. *SIAM J. Numer. Anal. 25(2)* (1988), 294–318.

[5] Einfeldt, B., Munz, C., Roe, P., and Sjgreen, B. On gudonov-type methods near low densities. *J. Comput. Phys. 92* (1991), 273–295.

[6] Godunov, S. A finite difference method for the computation of discontinuous solutions of the equations of fluid dynamics. *Comp. Math. (in Russian) 47* (1959), 357–393.

[7] Harten, A., Lax, P., and van Leer, B. On upstream differencing and gudonov-type schemes for hyperbolic conservation laws. *SIAM Review 25(1)* (1983), 35–61.

[8] LeVeque, R. J. *Finite Volume Methods for Hyperbolic Problems.* Cambridge Texts in Applied Mathematics, UK, 2002.

[9] Osher, S., and Solomon, F. Upwind difference schemes for hyperbolic conservation laws. *Math. Comp. 38,158* (1982), 339–374.

[10] Richtmyer, R., and Morton, K. *Difference Methods for Initial Value Problems.* Interscience-Wiley, New York, 1967.

[11] Roe, P. Approximate riemann solvers, parameter vectors, and difference schemes. *J. Comput. Phys. 43* (1981), 357–372.

[12] Roe, P. Numerical algorithms for the linear wave equation. Technical Report 81047, Royal Aircraft Establishment, Bedford, UK, 1981.

[13] Roe, P. L. Characteristic-based schemes for the euler equations. *Ann. Rev. Fluid Mech. 18* (1986), 337.

[14] Rusanov, V. Calculation of interaction of non-steady shock waves with obstacles. *J. Comput. Math. Phys. USSR 1* (1961), 267–279.

[15] Sod, G. A survey of several finite difference methods for systems of nonlinear hyperbolic conservation laws. *J. Comp. Phys. 27* (1978), 1–31.

[16] Sweby, P. Exact riemann solver. University of Reading, UK, 2011.

[17] Toro, E. A linearised riemann solver for the time-dependent euler equations of gas dynamics. *Proc. Roy. Soc. London A434* (1991), 683–693.

[18] Toro, E. On glimm-related schemes for conservation laws. Technical Report 97-02, Department of Mathematics and Physics, Manchester Metropolitan University, UK, 1997.

[19] Toro, E., Spruce, M., and Speares, W. Restoration of the contact surface in the hll-riemann solver. *Shock Waves 4* (1994), 25–34.

[20] Toto, E. *Riemann Solvers and Numerical Methods for Fluid Dynamics: A Pratical Introduction.* Springer, UK, 1999.

[21] van Leer, B. Towards the ultimate conservative difference scheme ii: Monotonicity and conservation combined in a second order scheme. *J. Comp. Phys. 14* (1974), 361–370.

[22] Woodward, P., and Colella, P. The numerical simulation of two-dimensional fluid flow with strong shocks. *J. Comput. Phys. 54* (1984), 115–173.